OXFORD

# Formation of Chromitite Seams and Associated Anorthosites in Layered Intrusion by Reactive Volatile-rich Fluid Infiltration

Jennifer S. Marsh<sup>1</sup>, Michael J. Pasecznyk<sup>2</sup> and Alan E. Boudreau (b) 1\*

<sup>1</sup>Division of Earth & Ocean Sciences, Nicholas School of the Environment, Box 90328, Duke University, Durham, NC 27708, USA; <sup>2</sup>Sibanye-Stillwater Mining Co., Nye, MT 59061, USA

\*Corresponding author. Telephone: 919-740-7727. Fax: 919-613-8061. E-mail: Boudreau@duke.edu

Received 23 July 2020; Accepted 5 December 2020

# **ABSTRACT**

Drilling related to development of the platinum-group element deposit of the J-M Reef of the Stillwater Complex returned samples of a rare chromitite seam between anorthosite and norite in a discordant anorthositic body. Plagioclase core An concentrations are marginally higher and modestly reversely zoned on the norite side (average  $An_{core} = 83.8$ ; average  $An_{core} - An_{rim} = -1.1$ ) as compared with the anorthosite side (average  $An_{core}$  82.5; average  $An_{core} - An_{rim} = +1.0$ ). The anorthosites are also characterized by a slightly smaller average plagioclase grain size than plagioclase in the norite (1.41 mm and 1.54 mm, respectively). The chromite can contain single and polyphase inclusions of orthopyroxene, plagioclase, amphibole, biotite and Cl-rich apatite. These and other compositional and textural features, as well as inference from other discordant anorthositic bodies in the Banded series, are all consistent with a chromatographic model of chromite precipitation at a reaction front as a norite protolith reacts with a CI-rich aqueous fluid saturated in plagioclase alone. Chromitite seam formation is modeled using an infiltration metasomatic model, in which a fluid becomes progressively undersaturated in pyroxene as it rises into the hotter part of the crystal pile. As this pyroxene-undersaturated fluid moves through a noritic protolith, it dissolves the Cr-bearing orthopyroxene to produce an anorthosite. Chromite precipitates at the reaction front between the anorthosite and the norite owing to liberation of Mg and Cr from pyroxene. Continuous redissolution and reprecipitation of chromite occurs as the pyroxene dissolution front moves in the direction of fluid flow, collecting the Cr lost from the anorthosite. Owing to Cr dissolved mainly as a neutral divalent cation complex, CrCl(OH)<sup>0</sup>, in the solution, but incorporated as a trivalent cation in chromite, the required redox reaction can involve concurrent precipitation of sulfide with chromite. This mechanism differs from some recent models in that the anorthosites are themselves replacement bodies and are not original precipitates from a magma nor formed by loss of mafic material by partial melting. The results show the need for experimental mineral solubility data at T and P conditions appropriate to upper crustal mafic-ultramafic intrusions.

Key words: Stillwater Complex; infiltration metasomatism; chromitites

# INTRODUCTION

The petrogenesis of chromitites presents several problems in layered intrusion research. A role of volatiles is suggested by the not uncommon occurrence of polymineralic inclusions in chromite, including Cl-bearing hydrous minerals, that have been interpreted to have crystallized from hydrous and possibly fluid-saturated silicate liquid inclusions (e.g. Spandler et al., 2005). [In this paper, fluid will refer to a volatile-rich (C–O–H–S–Cl) supercritical solution, and liquid will refer to a silicate liquid or silicate melt phase.] Other problems include the apparent crystallization of locally thick layers (of the order of  $\sim 1\,\mathrm{m}$ ) of Cr-rich spinel alone from a magma that contains only minor amounts of Cr. Where

chromitites are present as much thinner (~1 cm) seams, they may be present at boundaries between contrasting rock types, in many cases between an anorthositic rock and a more mafic or ultramafic assemblage. The chromitite seams can occur as relatively flat horizontal layers, but it is not uncommon for the chromitites to define non-planar, dimpled, undulatory or strongly discordant contacts between contrasting lithologies. Those from the Rum intrusion (O'Driscoll et al., 2010) and those associated with the potholes in the Merensky Reef and the MG2 chromitite of the Bushveld Complex (Cawthorn, 2015) are particularly good examples of non-planar and discordant chromitites. Contacts with surrounding rocks are typically sharp, within a few chromite grain diameters, and the seams may separate rocks that contain little or no chromite or contain chromite on one side alone. The common association with anorthositic rocks adds an additional complication in that it again requires the formation of a nearmonomineralic anorthosite as do the chromitites themselves. They can be of economic importance owing to the common association with platinum-group element (PGE)-rich sulfides.

Models for the crystallization of chromitites range from a variety of direct crystallization from chromitesaturated magmas and magma mixing schemes, mechanical emplacement of chromite-rich mushes and pressure fluctuations, to a variety of infiltration-reaction metasomatic processes and the importance of volatiles. In regard to the non-planar irregular chromitite seams that develop between anorthositic rocks and more mafic rocks, there have been a number of proposed formation mechanisms. O'Driscoll et al. (2009, 2010) suggested that the downward percolation and remelting by a hot picritic magma into a troctolite mush in the Rum Intrusion forced the contaminated picrite to become saturated in chromite and left a chromitiferous anorthositic residue. Formation of a chromitite seam was assumed to have been aided by deformation of a mush and the migration and trapping of chromite seed crystals at lithological contacts. Scoon & Costin (2018) suggested that thin chromitites in the Upper Critical Zone of the Bushveld Complex were the result of incongruent partial melting of a relatively Cr-rich norite as the result of the intrusion of a thin sill of hot ultramafic magma into an existing norite-anorthosite assemblage. Veksler & Hou (2020) suggested that it was the addition of H<sub>2</sub>O into the chamber that induced hydration melting of the floor rocks to produce chromitites of the Critical Zone of the Bushveld Complex. Latypov et al. (2017) suggested that chromitite seams that occur at the floor and side margins of anorthositic potholes in the Merensky Reef of the Bushveld Complex formed by the emplacement of superheated, dense magma along the base of the chamber that led to erosional melting of the floor, followed by the in situ crystallization of chromite on the bottom and sides of the resulting potholes.

In contrast to these magmatic or remelting models are metasomatic models involving infiltration of

reactive silicate liquid. Mathez & Kinzler (2017) suggested that chromitite seams can form as metasomatic reaction zones that develop between a hydrated silicate melt and a crystal mush. Nikolaev et al. (2020) suggested that chromite solubility in a silicate liquid is a function of the liquid's pyroxene component concentration and thus chromite can be dissolved and reprecipitated during compaction-driven migration of interstitial liquids. The concentrating process involves Cr-spinel dissolution into liquids enriched in pyroxene components and the subsequent redisposition of chromite where the Cr-rich liquid reacts with anorthositic layers or horizons enriched in olivine. Finally, Kaufmann et al. (2020) suggested a multistage magma replenishment model that involved aspects of a number of the above ideas.

Not generally considered in the metasomatic models is the possibility that the metasomatic agent is a fluid and not a silicate liquid. Yardley (2005) noted that solution concentrations in crustal fluid inclusions in general increase with both temperature and Cl content (e.g. Fe reaching 10 wt% at 700 °C in the more Cl-rich solutions), evidence that they can be potent metasomatizing agents. Studies from the Stillwater Complex demonstrated the existence of a variety of Cl-rich fluid inclusions present in the lower parts of the complex, ranging from halide melts (>82 wt% NaCl<sub>equiv</sub>) to compositionally variable brines that can contain up to 10 different daughter minerals (Hanley et al., 2008). Apatite stratigraphically associated with these fluid inclusions can be composed of 100 mol% chlorapatite (Boudreau & McCallum 1989). These unusually Cl-rich apatite compositions are in contrast to the Cl-poor compositions from many other intrusions that commonly average <20 mol% chlorapatite and more typically less than 10 mol% chlorapatite (e.g. Boudreau, 2016). Mathez & Webster (2005) noted that CI has limited solubility in silicate liquids; once the melt becomes saturated in CI, additional CI enrichment during crystallization of anhydrous minerals must be accommodated by coexisting fluid, apatite, or other phases rather than the liquid. All of this suggests that a Cl-rich fluid was circulating throughout the lower parts of the Stillwater Complex during solidification.

Such Cl-rich fluids have been called upon to describe a number of zoned and unzoned discordant anorthositic bodies that replace gabbro and gabbronorite in the Stillwater Complex and in other layered intrusions. These include the 'pillow troctolite' described by Hess (1960) and the discordant zoned anorthosite—troctolite bodies described by Meurer et al. (1997), where the gabbronorite host is replaced by troctolite and then by anorthosite by progressive loss of the mafic components to an infiltrating Cl-rich hydrous fluid. A metasomatic model was also suggested by McBirney & Sonnenthal (1990) and Sonnenthal (1992) to explain discordant anorthosite bodies replacing gabbro protolith in the Skaergaard Intrusion.

This paper describes the petrology and compositional features associated with a chromitite seam developed between a leuconorite and a discordant anorthosite body associated with the platiniferous J-M Reef from the Lower Banded series of the Stillwater Complex, Montana. Following the interpretation of Meurer et al. (1997) and Baker & Boudreau (2019), it is suggested that Cl-bearing, aqueous fluids, initially exsolved from deeper, cooler parts of the crystal pile, will become undersaturated in the more soluble pyroxene components as they move up into hotter parts of the pile such that the fluid becomes saturated in plagioclase alone. A model is proposed by which the discordant anorthosite and chromitite both develop as metasomatic replacement lithologies as this reactive, pyroxene-undersaturated fluid reacts with a norite protolith.

# GENERAL GEOLOGY OF THE STILLWATER COMPLEX AND ITS CHROMITITES

The Stillwater Complex is a  $2701\pm8\,\text{Ga}$  (DePaolo & Wasserburg, 1979) layered, ultramafic-mafic intrusion located in south-central Montana on the north side of the Beartooth Mountains (Fig. 1). The Stillwater magma intruded regionally metamorphosed metasedimentary rocks as a subvolcanic or perhaps sub-flood basalt sill

at a depth of about 6–7 km. The intrusion heated the surrounding country rocks to produce a metamorphic aureole 2–3 km thick (Helz, 1995; Labotka & Kath, 2001). The upper portion of the Stillwater was eroded before the mid-Cambrian and then covered by Paleozoic sediments. Movement from the Laramide orogeny event created the current steep dip of  $\sim\!70^\circ$  (and locally overturned) to the NNE. The exposed rock in the Stillwater Complex is about 6.5 km in maximum stratigraphic thickness, with a 45 km strike length.

The Stillwater Complex has been informally subdivided into three major stratigraphic divisions and numerous subdivisions based on major rock types; from the base upward, the major divisions are the Basal series, the Ultramafic series, and the Banded series, and they are described as follows (Fig. 2).

Much of the Basal series is lost or obscured owing to post-emplacement faulting, but the first appearance of laterally continuous norite signifies the lowest unit in the Stillwater Complex. It is at maximum about 400 m thick, but more commonly between about 60 and 240 m. The norite is broadly upward modally graded, defined by irregularly decreasing plagioclase to orthopyroxene ratio (Raedeke & McCallum, 1984).

The first appearance of a significant amount of olivine-bearing rocks marks the base of the Ultramafic series. It is divided into a lower unit, the Peridotite zone,

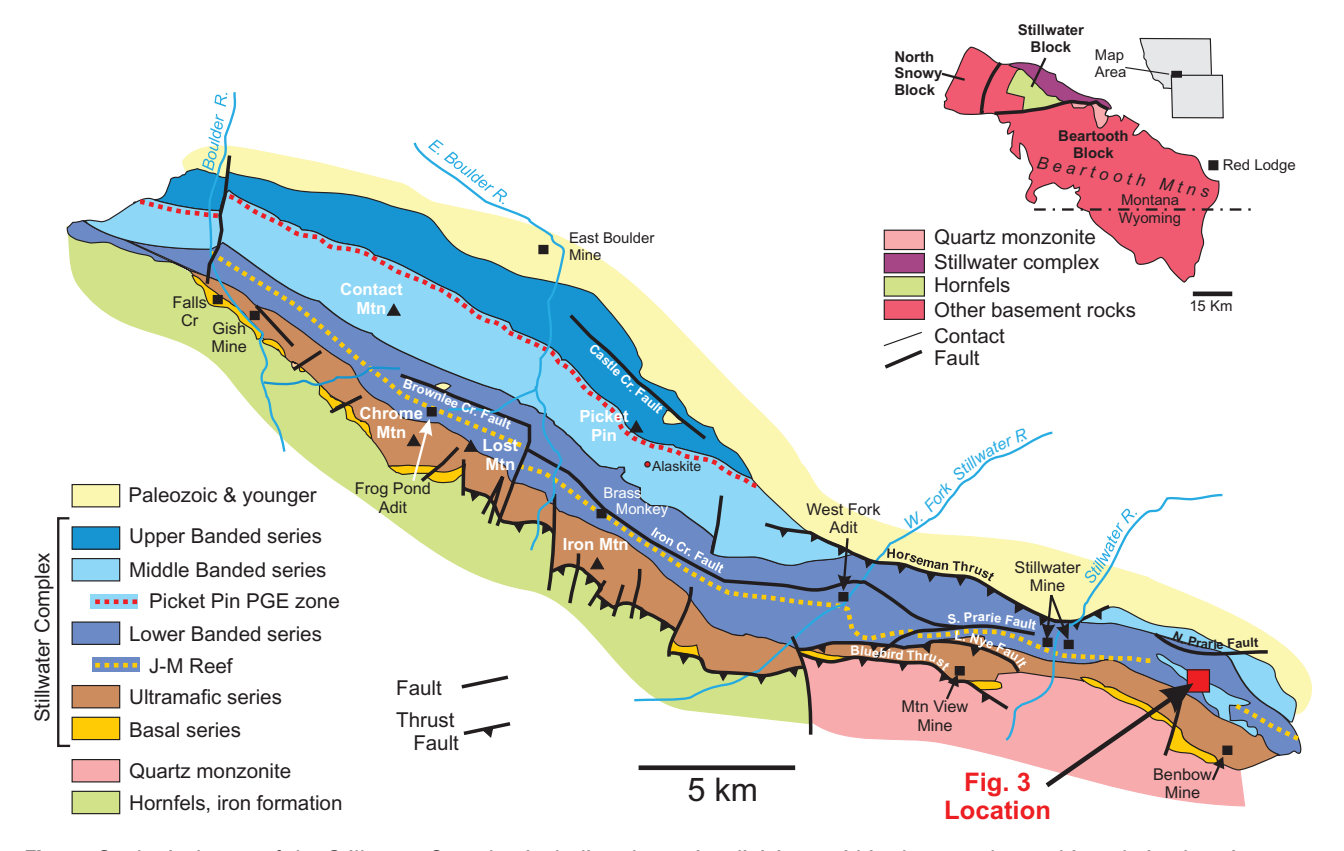


**Fig. 1.** Geological map of the Stillwater Complex including the major divisions within the complex and its relative location compared with the surrounding geology. Black squares are mine locations and small black isolated triangles are the summits of named mountains. Locations of the drill holes and samples shown in Fig. 3 are also shown. After Jones *et al.* (1960) and McCallum *et al.* (1999), with permission.

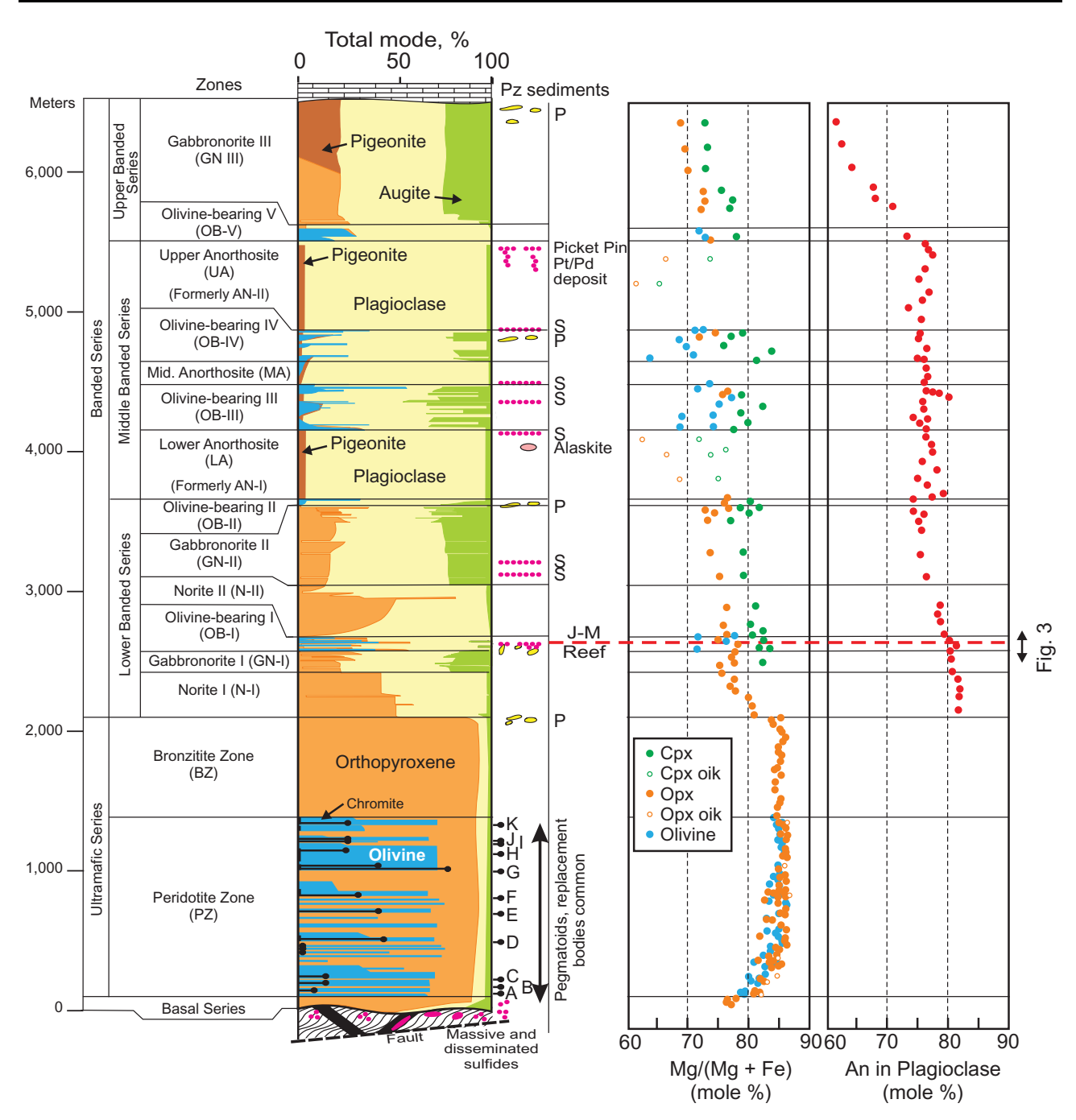


**Fig. 2.** Major stratigraphic units (formal and informal), mineral modes, and mineral compositional trends as a function of stratigraphic height in the Stillwater Complex. Modal olivine in poikilitic and granular harzburgite from the Ultramafic series is in part schematic, based on average modes. Also shown are the locations of the A–K chromitites (labeled 'A'–'K'), zones where pegmatoids and sulfides are common (labeled 'P' and 'S', respectively), the alaskite body described by Czamanske *et al.* (1991), and the locations of the J-M reef and the Picket Pin PGE zone (labeled). Modified after McCallum (1996), with permission.

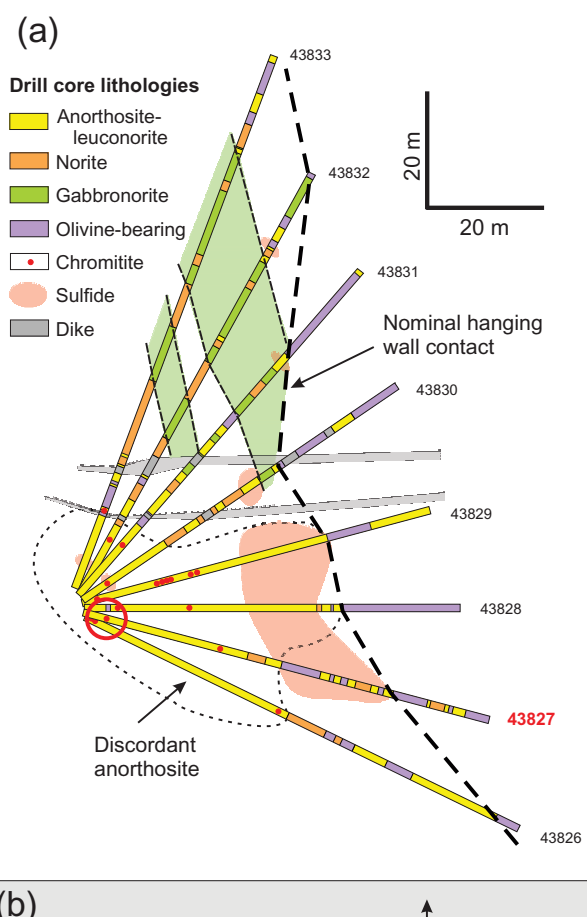
and an upper unit, the Bronzitite zone. The modest mineral compositional variation in the Ultramafic series has been interpreted to indicate several repetitions of magma influxes and minor venting of fractionated magma (McCallum 1996). The lower Peridotite zone is made up of a repeating sequence of peridotite or poikilitic harzburgite → granular harzburgite → orthopyroxenite; this cycle repeats 21 times at Mountain View. Chromitite seams in the Stillwater Complex are found

in the Ultramafic series near the bottom of many of these repeating cyclic units. They are labeled A and K from the bottom up, although some chromitite seams may be found in the Bronzitite zone at the very top of the Ultramafic series. The Bronzitite zone mainly consists of a uniform orthopyroxenite with interstitial augite and plagioclase, with minor amounts of chromite, quartz and, more rarely, apatite and biotite (Raedeke & McCallum, 1984; Boudreau 2016).

The Banded series of the Stillwater Complex consists of mainly plagioclase-rich rocks (norite, gabbronorite, troctolite and anorthosite). There are three generally recognized subdivisions within the Banded series: the Lower, Middle and Upper Banded series, each of which is further subdivided into a number of zones and subzones that vary between different researchers. Those used here are based on McCallum et al. (1980), as modified by Boudreau (2016). The top and bottom of the Middle Banded series are defined by two unusually coarse-grained anorthosite units up to 600 m thick. Olivine-bearing zone I (OB-I) of the Lower Banded series hosts the J-M Reef, an economic deposit of PGE- and sulfide-bearing rocks. OB-I itself is characterized by a stratigraphically and laterally variable package of norite, gabbronorite, anorthosite and olivine-bearing lithologies. It is the presence of an unusual chromitite seam developed between a leuconorite and anorthosite associated with the J-M Reef that is studied here.

# An unusual vertical chromitite seam from OB-I

Definition drilling by the Sibanye-Stillwater Mining Company for mine development is typically done as a fan of drill core drilled normal to regional strike of the layering and is designed to intercept the steeply dipping J-M Reef approximately every 15 m in both the horizontal and vertical directions. One vertical drill fan, located about 4.5 km east of the Stillwater River, intersected a number of thin chromitite seams that are oriented approximately normal to regional layering (Fig. 3a), all hosted in anorthositic or otherwise strongly leucocratic rocks. The longer ~1 cm wide chromitite intercepts ran for a distance of just over a meter down the center of the core. Regional layering dips steeply to the north, and the core was drilled at an angle of about 90° to regional strike of the layering. Drilling has shown that the anorthositic rocks that host the chromitites define a large discordant body just below the bottom of a larger, pothole-like feature, the latter being defined by leucocratic hanging-wall lithologies (typically anorthosites and leuco-troctolite with grain size about half that of the underlying rocks) that drop down and displace underlying OB-I lithologies (norite, gabbronorite and olivinebearing rocks). The discordant anorthosite is itself well mineralized just below this contact. Within this disturbed area, however, lithologies are difficult to correlate, even from one hole to the next. Rotating the section back to subhorizontal, the drill core-parallel chromitite seams define near-vertical contacts within this discordant anorthosite body, similar to marginal seams seen in Bushveld potholes (e.g. Latypov et al., 2017). Potholelike features where one lithology shows an abrupt lateral change to another are not uncommon in OB-I. Although disseminated chromite is common in the olivine-bearing lithologies of OB-I, well-defined chromitite seams are only rarely observed (≪1% of drill holes); some experienced mine geologists have seen



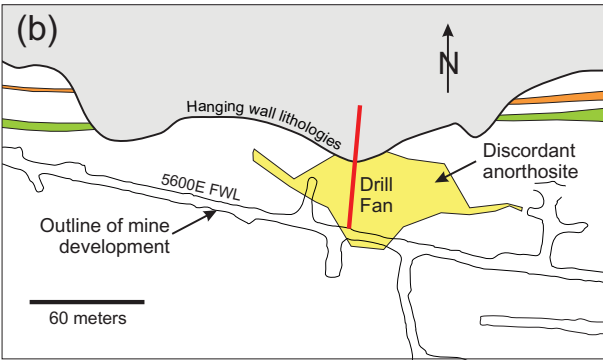


Fig. 3. (a) Vertical drill hole fan drilled roughly north-south (north is toward the right) and designed to intercept the J-M Reef at roughly 15 m centers. Whereas drilling intercepted a section normal to regional strike in the upper half of the drill fan, the drilling in the lower part of the fan intersected an anorthositic package of rock where lithological boundaries ran roughly parallel to the drilling direction. The associations of chromitite and extensive mineralization with anorthositic rocks should be noted. Circled area shows location of the chromitite seam from drill hole #43827 shown in Fig. 4. (b) Plan level map of the geology as defined by these and other drill holes (not shown for clarity). Because of the steep regional dip of the igneous layering, the plan map shows a stratigraphic cross-section; stratigraphic 'up' is to the north. It should be noted that the anorthositic body hosting the chromitite seams is developed beneath a larger pothole-like feature where hanging-wall lithologies displace underlying rocks.

them in only one or two other disturbed areas similar to that described here.

Fractures and subsequent alteration tend to be focused along some of the seams; however, the core section containing the chromitite seam studied here is about 20 cm long and relatively fresh. The seam separates an anorthosite (containing <10 % pyroxene) from a (leuco)norite. The drill core and scans of petrographic thin sections of the sampled section are shown in Fig. 4 and illustrate the curvilinear nature of the seam. The oikocrystic nature of the norite has led it to be logged as a 'oikocrystic anorthosite' by Stillwater mine geologists, whereas the interstitial nature of the pyroxene in the anorthosite is logged as an 'intercumulus anorthosite'. Here, these two rock types are simply described as norite and anorthosite, respectively.

In detail, the norite is composed of  $\sim 30\,\%$  poikilitic orthopyroxene and lesser clinopyroxene enclosing plagioclase. The plagioclase chadacrysts are euhedral to subhedral. The anorthosite on the other side of the

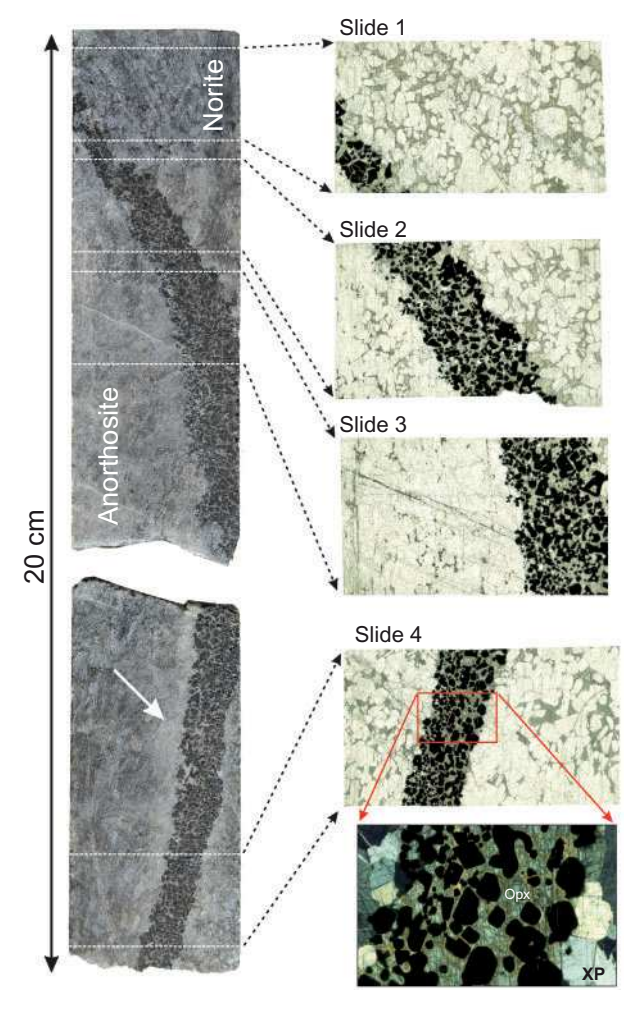


Fig. 4. Set of four petrographic thin sections from an  $\sim$ 20 cm length of drill core #43827 that ran near-parallel to a curved chromitite seam separating anorthosite (on the left side of core) from a norite (on the right). Arrow on the drill core points to selvage of nearly pure plagioclase adjacent to the chromitite seam. The chromitite seam is composed of chromite poikilitically enclosed in orthopyroxene (as seen in the crossed-polarizers detail view of Slide 4); white areas in the chromitite seam are not plagioclase but plucked mineral grains.

chromitite is composed of ≥90% plagioclase with an equigranular-mosaic texture. The interstitial mineralogy is composed of approximately equal amounts of orthopyroxene and clinopyroxene, both occurring either as interstitial space filler or as thin, skeletal oikocrysts. Locally, a nearly pure anorthosite selvage is present immediately adjacent to the chromitite seam. The chromitite seam itself is composed of about 60% chromite enclosed in optically continuous interstitial-poikilitic orthopyroxene; plagioclase is notably absent except as inclusions in chromite. The seam has a variable width, typically ranging between  $\sim 0.5$  and 1.5 cm. Boundaries with the norite and anorthosite are sharp, but a few isolated small chromite grains can be found just into the anorthosite. The chromite grains in the seam occur both as individual grains and as partially annealed multigrain clusters.

A variety of monomineralic and polymineralic inclusions,  $100-300\,\mu m$  in size, are common in chromite, particularly in the large agglomerated grains. There are two main types. The first type is composed of a mixed population of orthopyroxene and magnesio-hornblende with minor impure or altered biotite (phlogopite) and Cl-rich apatite (Fig. 5a and b). Hydrous minerals are otherwise rare or absent in the interstitial mineral assemblage. These inclusions are similar to hydrous mineral-rich inclusions seen in chromite from

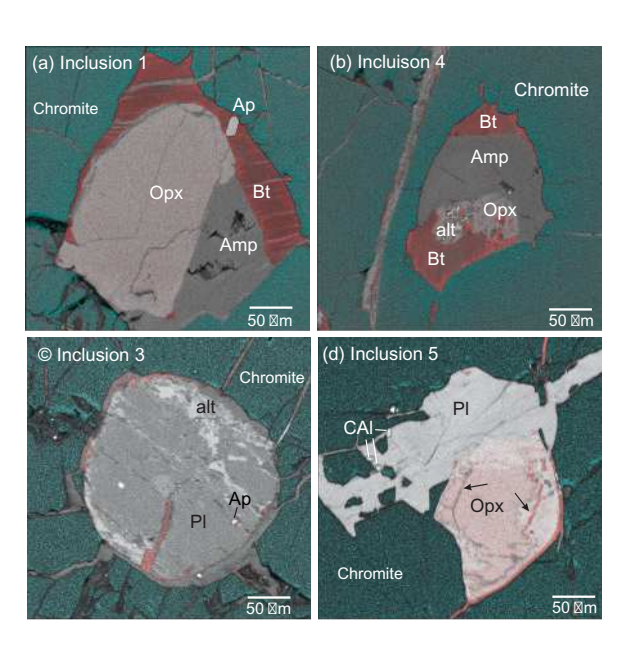


Fig. 5. Composite electron microprobe X-ray maps of inclusions in chromite. Pl, plagioclase; Opx, orthopyroxene; Amp, amphibole (Na-rich magnesio-hornblende); Bt, biotite (phlogopite); Ap, apatite; Cal, calcite; alt, undifferentiated alteration. (a) Polymineralic inclusion composed of a large orthopyroxene grain as well as amphibole, impure or altered biotite and apatite. (b) Polymineralic inclusion composed of amphibole, orthopyroxene, impure or altered biotite, apatite and a patch of undifferentiated alteration. (c) Inclusion composed mainly of a single rounded plagioclase grain (locally altered) and trace apatite. (d) Irregular inclusion composed of plagioclase and orthopyroxene with minor calcite (alteration?). Arrows in orthopyroxene indicate possible original grain boundary.

elsewhere in OB-I (e.g. Boudreau, 1999a) and from the G chromitite of the Peridotite zone (e.g. Spandler et al., 2005). The second type is composed of plagioclase  $\pm$  orthopyroxene (Fig. 5c and d) without any significant volatile-bearing minerals. The grains can be rounded to irregular.

#### **METHODS**

Analysis of individual plagioclase, pyroxene and chromite grains was carried out on the four polished thin sections shown in Fig. 4 using the Duke Cameca Camebax electron microprobe using a variety of synthetic and natural mineral standards. Standard analytical conditions were 15 keV acceleration voltage, 15 and 20 nA beam current for plagioclase and pyroxene–chromite, respectively, and a beam defocused to 10  $\mu m$ , with standards checked every 10–15 grains. Data were corrected using a Phi-Rho-Z correction routine (Bastin et al., 1996). Anorthite content of plagioclase (An) is reported as An = an/(an + ab + or).

Crystal size distribution analysis was carried out on slides 1 and 3 for plagioclase and slide 2 for chromite. Grains of plagioclase were traced from photomicrographs using both plane-polarized and crossed polarizer views; partial grains at the margins of the sections were not included. These tracings were then scanned and centerline traces were made using Corel Draw® v. 17 to produce a uniform line width. Individual grains were then filled with color. For chromite, their opaque nature made image analysis of the photomicrograph easier. Plucked regions with typical chromite habit were filled with black and included, and agglomerated grains were separated into sub-grains where original boundaries could be reasonable inferred, otherwise they were included with the largest grain size fractions. For both plagioclase and chromite, crystal sizes were found using the particle analysis routine of Image J<sup>®</sup>. Grain sizes were calculated as the Feret diameter, defined as the diameter of a circular grain having the same area as the grain.

# **RESULTS**

#### **Plagioclase**

Just under 100 plagioclase core–rim analyses were obtained and typical analyses are listed in Table 1. (complete datasets are available in the Supplementary Data and are available for downloading at http://www.petrology.oxfordjournals.org). Three analyses with unusually high Fe were not plotted as they were assumed to have inadvertently hit an inclusion or to have been affected by marginal mafic grains. Plagioclase trends on each side of the chromitite seam are shown in Fig. 6 as a function of distance to the center of the seam. Figure 7 shows histograms of An<sub>core</sub> and An<sub>core</sub> – An<sub>rim</sub> compositions in both the norite and anorthosite. Plagioclase in the anorthosite tends to be preferentially normally zoned, whereas that in norite tends to be

reversely zoned, the An<sub>core</sub> – An<sub>rim</sub> differences averaging 1·0 and –1·1, respectively (Figs 6b and 7c, d). Plagioclase core values tend to be modestly higher in the norite as compared with the anorthosite, with average cores values of 83·8 and 82·5, respectively (Fig. 6a). Otherwise the plagioclase core compositions significantly overlap, with the lower average of the anorthosite plagioclase skewed to low An compositions typical of the anorthosite plagioclase rims and the norite plagioclase average skewed to the higher An compositions typical of the norite plagioclase rims (Fig. 7a and b). This is perhaps to be expected, as one is never sure how close to the rim a 'core' analysis is in the third dimension, particularly for the smaller grains.

For minor elements in plagioclase (Fig. 6c), there is a modest higher Fe<sub>total</sub> (as FeO) in plagioclase from the anorthosite (average 0.41 wt% FeO) as compared with the norite (average 0.36 wt% FeO), except in the vicinity of the chromitite seam, where FeO is markedly lower in both the anorthosite and the norite. The plagioclase in the anorthosite has a marginally higher K<sub>2</sub>O concentrations compared with the norite, consistent with the lower An content of the plagioclase in the anorthosite.

Crystal size distributions for plagioclase are shown in Fig. 8. The histograms of plagioclase grain size are broadly similar in both the norite and the anorthosite, with the plagioclase in the norite containing a modestly larger proportion of larger grains that skews the average Feret grain diameter to a slightly higher value as compared with the anorthosite (1.54 mm vs 1.41 mm, respectively). The modes (most frequent) of the grain sizes are otherwise similar.

#### Pyroxene

Microprobe analyses of pyroxene are shown in Fig. 9 and typical values listed in Table 2. Orthopyroxene interstitial to chromite in the seam has a consistently higher Mg# (average ~84) than the orthopyroxene in the anorthosite or norite. Orthopyroxene in the norite quickly drops over a distance of about 1cm from the seam to Mg# of ~77, which is more typical of orthopyroxene from the gabbronorite subzone of OB-I (Todd *et al.*, 1982). Orthopyroxene in the anorthosite also tends to more Fe-rich compositions immediately next to the chromitite seam with more variable but more Mg-rich compositions away from the seam, but analyses are few.

 ${\rm Cr_2O_3}$  concentrations of both orthopyroxene and clinopyroxene show no clear trends, with some having typical gabbronorite subzone concentrations of 0.4 wt%  ${\rm Cr_2O_3}$  reported by Todd *et al.* (1972) and others being at or below nominal detection levels.

#### Chromite

There is little difference in compositions of the chromite grains across the chromitite seam (Table 3). Compared with typical chromite from the G chromitite unit of the Ultramafic zone, the seam has a lower Mg# than the G

Table 1: Selected plagioclase electron microprobe analysis

| Analysis:            | 1               | 2            | 3         | 4        | 5            | 6      | 7      | 8      |
|----------------------|-----------------|--------------|-----------|----------|--------------|--------|--------|--------|
| ID:                  | 5 core          | 5 rim        | Incl core | Incl rim | 1 core       | 1 rim  | 2 core | 2 rim  |
| Rock:                | Anorth          | Anorth       | Chmt      | Chmt     | Norite       | Norite | Norite | Norite |
| Distance (mm):       | -5.0            | <b>-5</b> ⋅0 | 0.0       | 0.0      | 5.0          | 5.0    | 13.7   | 13.7   |
| SiO <sub>2</sub>     | $46.9 \pm 0.4$  | <b>45</b> ⋅8 | 47.0      | 46.5     | 46.6         | 44.8   | 47·0   | 47.4   |
| $Al_2\bar{O}_3$      | $34.0 \pm 0.2$  | 34.5         | 33.5      | 34.2     | 33.6         | 34.3   | 33.8   | 33.6   |
| FeO <sub>total</sub> | $0.27 \pm 0.1$  | 0.16         | 0.23      | 0.32     | 0.40         | 0.29   | 0.41   | 0.43   |
| MgO                  | $0.02 \pm 0.02$ | n.d.         | n.d.      | n.d.     | 0.02         | n.d.   | n.d.   | n.d.   |
| CaO                  | $17.7 \pm 0.1$  | 18.1         | 17.4      | 17.9     | <b>17</b> ⋅1 | 18⋅1   | 17·1   | 17⋅1   |
| BaO                  | $0.01 \pm 0.02$ | 0.02         | 0.01      | 0.03     | 0.04         | 0.03   | 0.02   | 0.05   |
| Na <sub>2</sub> O    | $1.87 \pm 0.07$ | 1.58         | 1.76      | 1.51     | 1.73         | 1.19   | 1.79   | 1.83   |
| $K_2\bar{O}$         | $0.05 \pm 0.02$ | 0.03         | 0.04      | 0.03     | 0.04         | 0.02   | 0.05   | 0.05   |
| Total                | 100⋅8           | 100-3        | 100.      | 100-4    | 99.5         | 98.8   | 100.1  | 100⋅5  |
| 100.8                | 100.3           | 100.         | 100.4     | 99.5     | 98.8         | 100.1  | 100.5  |        |
| An                   | 83.7            | 86.2         | 84.3      | 86.6     | 84.3         | 89.3   | 83.8   | 83.5   |
| Ab                   | 16.0            | 13.7         | 15.5      | 13.3     | 15⋅4         | 10⋅6   | 15⋅8   | 16.2   |
| Or                   | 0.3             | 0.2          | 0.2       | 0.2      | 0.3          | 0.1    | 0.3    | 0.3    |
| $Si + Al + Fe^{3+}$  | 3.969           | 3.970        | 3.986     | 3.985    | 3.995        | 3.987  | 3.996  | 3.996  |
| Ca + Na + K          | 1.029           | 1.030        | 1.014     | 1.014    | 1.004        | 1.013  | 1.003  | 1.003  |
| An                   | 83.7            | 86.2         | 84.3      | 86.6     | 84.3         | 89.3   | 83.8   | 83.5   |
| An(core-rim)         | <b>-2</b> ⋅5    |              | –2⋅3      |          | -4.9         |        | 0.4    |        |

Rock abbreviations: Anorth, anorthosite; Chmt, chromitite. Distance is in millimeters from center of chromitite seam (typically 1 cm thick); negative values are towards the anorthosite. n.d., not determined.

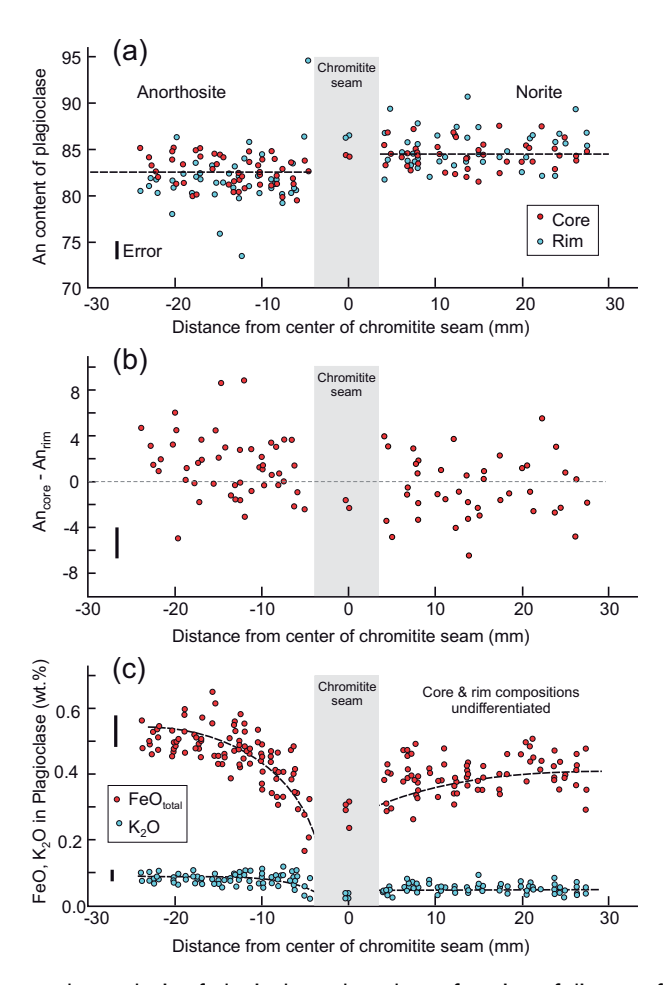


Fig. 6. Results from electron microprobe analysis of plagioclase plotted as a function of distance from the center of the chromitite seam. Negative distances are in the anorthosite, positive distance is in the norite. Two analyses of plagioclase in the chromitite seam are of plagioclase inclusions in chromite (core only). (a) Plot of the core (red circles) and rim (light blue circles) An compositions of plagioclase. (b) Plot of the core–rim An compositional differences; positive values are normally zoned, negative values are reversely zoned. (c) Plot of FeO (red) and K<sub>2</sub>O (light blue) in plagioclase (both core and rim, undifferentiated). Error bars are typical counting statistical error.

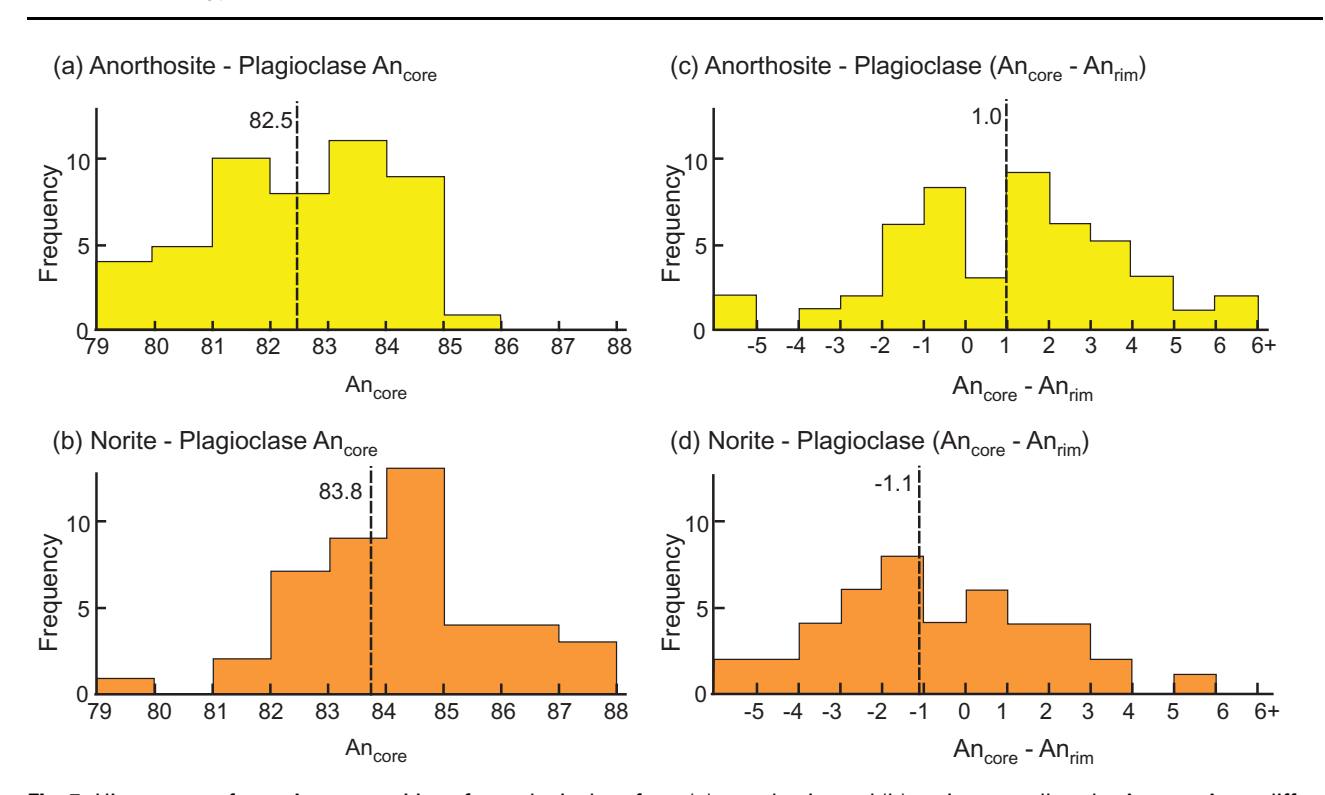


Fig. 7. Histograms of core An compositions from plagioclase from (a) anorthosite and (b) norite, as well as the  $An_{core} - An_{rim}$  difference in plagioclase from (c) anorthosite and (d) norite. Dashed lines and numerical values are the average for each plot.

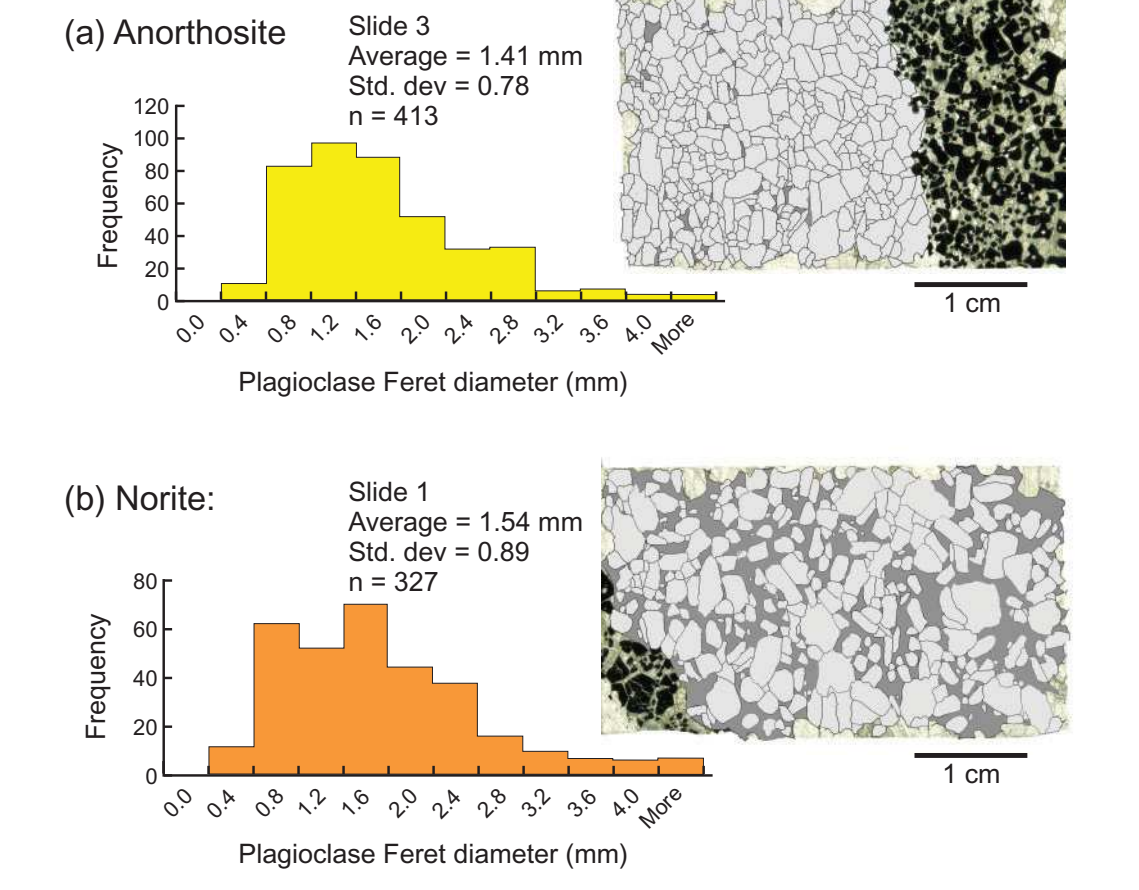


Fig. 8. Histograms of plagioclase grain sizes from (a) anorthosite (Slide 3) and (b) norite (Slide 1) on either side of the chromitite seam. Insets to each plot show the outlines of plagioclase grains used in the crystal size analysis (light grey, plagioclase; dark grey, pyroxene) overlain on the thin section photomicrograph. Partial grains on the edges of the section were not included.

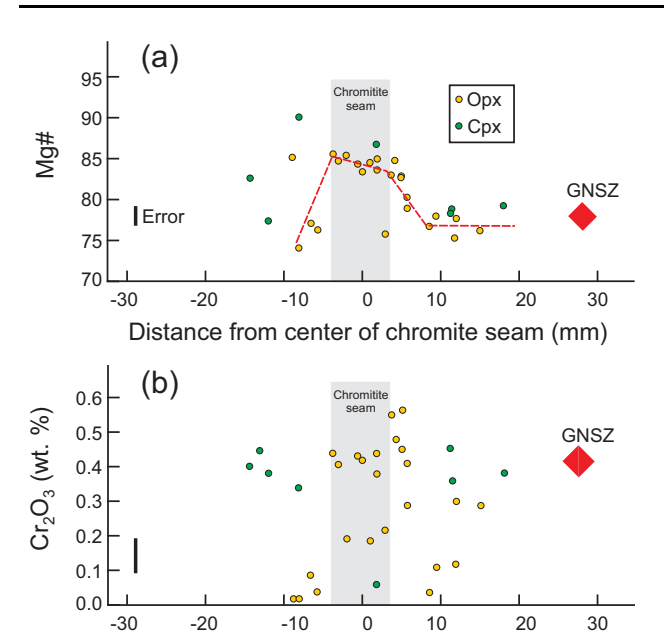


Fig. 9. Plot of (a) Mg# and (b) Cr<sub>2</sub>O<sub>3</sub> compositions of orthopyroxene (orange circles) and clinopyroxene (green circles). Both are plotted as a function of distance from the center of the chromitite seam; negative distances are in the anorthosite, positive distance is in the norite. The diamond labeled 'GNSZ' is an average orthopyroxene from the Gabbronorite subzone of Olivine bearing zone I, from Todd *et al.* (1982). Error bars are typical counting statistical error.

Distance from center of chromitite seam (mm)

chromitite (46 vs 53, respectively), and a slightly lower  $Cr_2O_3$  content [40 vs 45 wt%  $Cr_2O_3$ , respectively and corresponding to Cr#=100Cr/(Cr+AI) of 57 vs 59, respectively].

Crystal size distributions from the chromitite seam from Slide #2 are shown in Fig. 10. For chromite, the seam was divided roughly in half along the length of the seam and the CSD was determined for the half next to norite and the half next to anorthosite. Whereas the mode or most common size ranges are the same for both sides (the 0.2-0.4 mm size fraction), the average size on the norite side is almost 50% larger that of the anorthosite side (0.76 vs 0.53 mm, respectively; Fig. 10b and c). Furthermore, there are only about half as many grains on the norite side as compared with the anorthosite side (n = 166 vs n = 333, respectively). In part, this represents the tendency for the grains on the norite side to form large composite grains by the agglomeration of two or more smaller grains and the difficulty of estimating grain boundaries in the composite grains. The grain size distributions are otherwise skewed to the larger size range with few smaller grains typical of the bell-shaped curves common to chromite in layered intrusion and OB-I in particular (e.g. Waters & Boudreau, 1996).

#### Inclusion in chromite

The rare plagioclase in the chromite inclusions is similar in composition to plagioclase in the norite in both

core composition and being reversely zoned (Table 1, analysis 5 and 6). The orthopyroxene inclusions similarly fall within the compositional range of the interstitial-poikilitic orthopyroxene of the chromitite seam (Table 2, analysis 4). The amphibole is a Cl-poor magnesio-horn-blende (Table 4), similar to those reported from chromite inclusions elsewhere in the Stillwater Complex (Boudreau, 1999a; Spandler, 2005). Cl-poor phlogopite is not observed without being altered or otherwise poorly crystallized (Table 5, analysis 1). In contrast to the hornblende and phlogopite, apatite is distinctly Clrich (Table 5, analysis 2 and 3). The low Cl concentration in amphibole and mica relative to apatite is consistent with the strong Mg–Cl avoidance expected in these Mgrich minerals (Volfinger et al., 1985).

#### **DISCUSSION**

The chromitite described here does not occur as a typical layer-parallel seam as seen in the Ultramafic series but is instead associated with a large discordant anorthosite body that is itself located beneath a pothole-like feature developed in the J-M Reef. Although plagioclase is the dominant mineral on both sides of the seam, plagioclase is absent from the seam itself apart from that found in chromite inclusions. Plagioclase grains in the norite and anorthosite are roughly similar in size and there appears to be a modest but distinctly lower An content ( $\Delta$ An = -1·3) and higher  $K_2O$  and FeO plagioclase on the anorthosite side. Whereas plagioclase in the anorthosite tends to a modest normal zoning, that in the norite tends to a modest reverse zoning.

Chromite grains are more numerous and are less likely to form larger polygrain clusters on the anorthosite side. The abundance of hornblende and biotite in many inclusions is interpreted to have grown from a trapped hydrous silicate liquid, and suggests that the chromite grew in the presence of a relatively 'wet' and probably fluid-saturated environment. Spandler et al. (2005) reheated inclusions in chromite from the Ultramafic series that contained abundant hydrous minerals similar to those reported here. These melting experiments produced a vapor-saturated glass in many of the inclusions when quenched. For the Cl-rich apatite compositions reported in Table 5, the data of Mathez & Webster (2005) suggest that an aqueous fluid at 1066–1150 °C and ~0.2 GPa could contain in excess of 10 wt% Cl.

The few plagioclase grains entrained in chromite overlap the composition of plagioclase in the norite, consistent with these being chadacrysts or accidentally trapped inclusions. The rounded nature of the plagioclase inclusions and lack of plagioclase elsewhere in the chromitite implies that any plagioclase in the seam not trapped in chromite was unstable and lost during development of the seam.

Orthopyroxene in the seam has a markedly higher Mg# than that away from the seam, and FeO in both plagioclase and pyroxene decreases as the seam is

Table 2: Selected pyroxene electron microprobe analyses

| Analysis:   | 1               | 2            | 3      | 4             | 5      | 6      | 7      |
|---|-----------------|--------------|--------|---------------|--------|--------|--------|
| ID:   | 2-C             | 2-K          | 4-10   | 2-P           | 4-1    | 2-H    | 4-2    |
| opx/cpx:  | opx             | opx          | cpx    | opx<br>Charat | opx    | opx    | cpx    |
| Rock:   | Anorth          | Anorth       | Anorth | Chmt          | Norite | Norite | Norite |
| Distance (mm):  | <b>–</b> 5⋅7    | –8⋅1         | –12⋅00 | 1.9           | 2.90   | 15     | 11.40  |
| SiO <sub>2</sub>  | $54.4 \pm 0.5$  | <b>52</b> .7 | 52.7   | 55.3          | 54.4   | 53⋅6   | 52.5   |
| TiO <sub>2</sub>  | $0.38 \pm 0.18$ | 0.21         | 0.28   | 0.01          | 0.10   | 0.22   | 0.26   |
| $Al_2O_3$   | $0.83 \pm 0.13$ | 0.84         | 2.77   | 1.54          | 1.36   | 1.23   | 2.81   |
| Cr <sub>2</sub> O <sub>3</sub>  | $0.04 \pm 0.10$ | 0.02         | 0.38   | 0.38          | 0.22   | 0.29   | 0.36   |
| FeO   | $15.2 \pm 0.2$  | 17.4         | 7.8    | 10⋅4          | 15⋅8   | 16⋅1   | 7.50   |
| MnO   | $0.55 \pm 0.06$ | 0.31         | 0.15   | 0.09          | 0.30   | 0.25   | 0.19   |
| MgO   | $26.9 \pm 0.2$  | 25.8         | 15⋅2   | 31.0          | 26.4   | 26.9   | 15⋅6   |
| CaO   | $1.53 \pm 0.12$ | 0.74         | 20.9   | 0.78          | 2.11   | 0.81   | 20.4   |
| Na <sub>2</sub> O   | n.d.            | n.d.         | 0.27   | n.d.          | n.d.   | n.d.   | 0.24   |
| Total   | 99.8            | 98.0         | 100-4  | 99-4          | 100⋅7  | 99-4   | 99.9   |
| $\overline{X_{Wo}} = \text{Ca/(Ca} + \text{Mg} + \text{Fe}^{\text{T}})$ | 3.00            | 1.47         | 43.41  | 1.50          | 4.12   | 1.60   | 42.57  |
| $X_{En} = Mg/(Ca + Mg + Fe^{T})$  | 73.64           | 71.50        | 43.86  | 82.94         | 71.78  | 73.62  | 45.22  |
| $X_{E_S} = Fe^T/(Ca + Mg + Fe^T)$                                       | 23.35           | 27.03        | 12.72  | 15.56         | 24.09  | 24.79  | 12.22  |
| $Fe^{T}/(Fe^{T}+Mg)$  | 0.241           | 0.274        | 0.22   | 0.158         | 0.25   | 0.252  | 0.21   |
| $Fe^{2+}/(Fe^{2+}+Mg)$  | 0.237           | 0.258        | 0.22   | 0.151         | 0.24   | 0.238  | 0.21   |
| Mg#   | 0.763           | 0.742        | 0.78   | 0.849         | 0.76   | 0.762  | 0.79   |
| M2(VI)  | 1.000           | 1.000        | 1.00   | 1.000         | 1.00   | 1.000  | 1.00   |
| M1(VI)  | 1.000           | 1.009        | 1.00   | 1.000         | 1.00   | 1.001  | 1.00   |
| T(IV)   | 2.000           | 1.991        | 2.00   | 2.000         | 2.00   | 1.999  | 2.00   |

Distance is in millimeters from center of the chromitite seam; negative values are on the anorthosite side. Si and Al assigned to tetrahedral (T) site. Ca, Na, Mn, Fe<sup>2+</sup>, and Mg assigned to M2 octahedral site. Fe<sup>3+</sup>, Ti, Al, Fe<sup>2+</sup>, and Mg assigned to M1 octahedral site, (Fe<sup>2+</sup>/Mg) assumed the same in M1 and M2 sites.

approached. Mg–Fe exchange between chromite and a mafic silicate phase will re-equilibrate to produce a more Fe-rich chromite and a more Mg-rich silicate mineral during slow cooling (Irvine, 1965, 1967), and this appears to be the case here for pyroxene and the inclusion amphibole and phlogopite. The Fe-poor plagioclase next to the seam contains so little Mg that it is unlikely to represent Mg–Fe exchange between plagioclase and chromite but instead reflects the general loss of Fe to chromite in the local silicate liquid + volatile fluid environment during final solidification.

As noted in the Introduction, the wavy to discordant nature of the chromitite seams seen here and in the Bushveld and Rum intrusions has been attributed to either some sort of physical erosional process or a near-solidus to subsolidus metasomatic replacement mechanism. In regard to the former, a number of features of the seam make is incompatible with a number of existing models for direct precipitation at a sharp mush-magma interface. Models that envision that a chromitite and anorthosite can form by heating and remelting of a broadly horizontal norite by a hot magma (e.g. O'Driscoll et al., 2009; Scoon & Costin, 2018) would not work for a vertical seam where chromite would be expected to settle out from an advancing melt front. This also applies to those models that suggest that similar melting can occur by lowering the magma solidus by mixing an aqueous fluid with the magma in the chamber (e.g. Boudreau, 2016; Veksler & Hou, 2020). Those that suggest that the discordant anorthosite formed by initial erosion by the influx of a hot magma followed by chromite then plagioclase as the initial phase on the liquidus (e.g. Latypov et al., 2017) are

Table 3: Microprobe analysis of chromite from Slide 2

| Analysis:                      | 1                       | 2       | 3            |                               |
|--------------------------------|-------------------------|---------|--------------|-------------------------------|
| Grain:                         | Grain A                 | Grain B | Grain C      | G Cyclic<br>unit <sup>2</sup> |
| Distance (mm):                 | -4.6                    | -0.6    | 3.1          | _                             |
| TiO <sub>2</sub>               | $2.02 \pm 0.03$         | 1.72    | 1.59         | 0.45                          |
| $Al_2O_3$                      | $20.7 \pm 0.5$          | 20.1    | 20.7         | 19∙4                          |
| Cr <sub>2</sub> O <sub>3</sub> | $39.2 \pm 0.2$          | 40.5    | 40.9         | 44.5                          |
| Fe <sub>2</sub> O <sub>3</sub> | $6.27 \pm 0.2$          | 5.90    | 5.72         | 6⋅11                          |
| FeO                            | $20.9 \pm 0.2$          | 21.     | 20.9         | 16.6                          |
| MnO                            | $0{\cdot}2\pm0{\cdot}2$ | 0.2     | 0.2          | 0.19                          |
| NiO                            | n.d.                    | n.d.    | n.d.         | 0.10                          |
| MgO                            | $10.4 \pm 0.1$          | 10.     | 10.2         | 12.2                          |
| Total                          | 99.7                    | 99.4    | 100.1        | 99.6                          |
| Ti                             | 0.048                   | 0.041   | 0.038        | 0.011                         |
| Al                             | 0.773                   | 0.755   | 0.769        | 0.721                         |
| Cr                             | 0.981                   | 1.02    | 1.02         | 1.019                         |
| Fe <sup>3+</sup>               | 0.149                   | 0.142   | 0.136        | 0.145                         |
| Fe <sup>2+</sup>               | 0.554                   | 0.559   | 0.552        | 0.438                         |
| Mn                             | 0.005                   | 0.005   | 0.005        | 0.005                         |
| Mg                             | 0.488                   | 0.477   | 0.48         | 0.573                         |
| Mg#                            | 46.8                    | 46.0    | 46.5         | 54.3                          |
| Cr#                            | 55.9                    | 57·4    | <b>57</b> ⋅0 | 58.6                          |
| Tot. cat.                      | 3.000                   | 3.000   | 3.000        | 3.002                         |
| Tot. oxy.                      | 4.000                   | 4.000   | 4.000        | 4.000                         |

<sup>\*</sup>Duke University chromite standard from the G chromitite of the Stillwater Peridotite zone.

affected by density considerations: a superheated anorthositic magma without enough mafic component to be saturated in pyroxene would probably be of too low a density to flow along the floor of the magma chamber to induce melting. It also would require a rather fortuitous similarity of the plagioclase composition

Distance is from the center of the chromitite seam (typically 1 cm thick). Mg# = molar Mg/(Mg + Fe $^{2+}$ ) ratio; Cr# = molar Cr/ (Cr + Al) ratio.

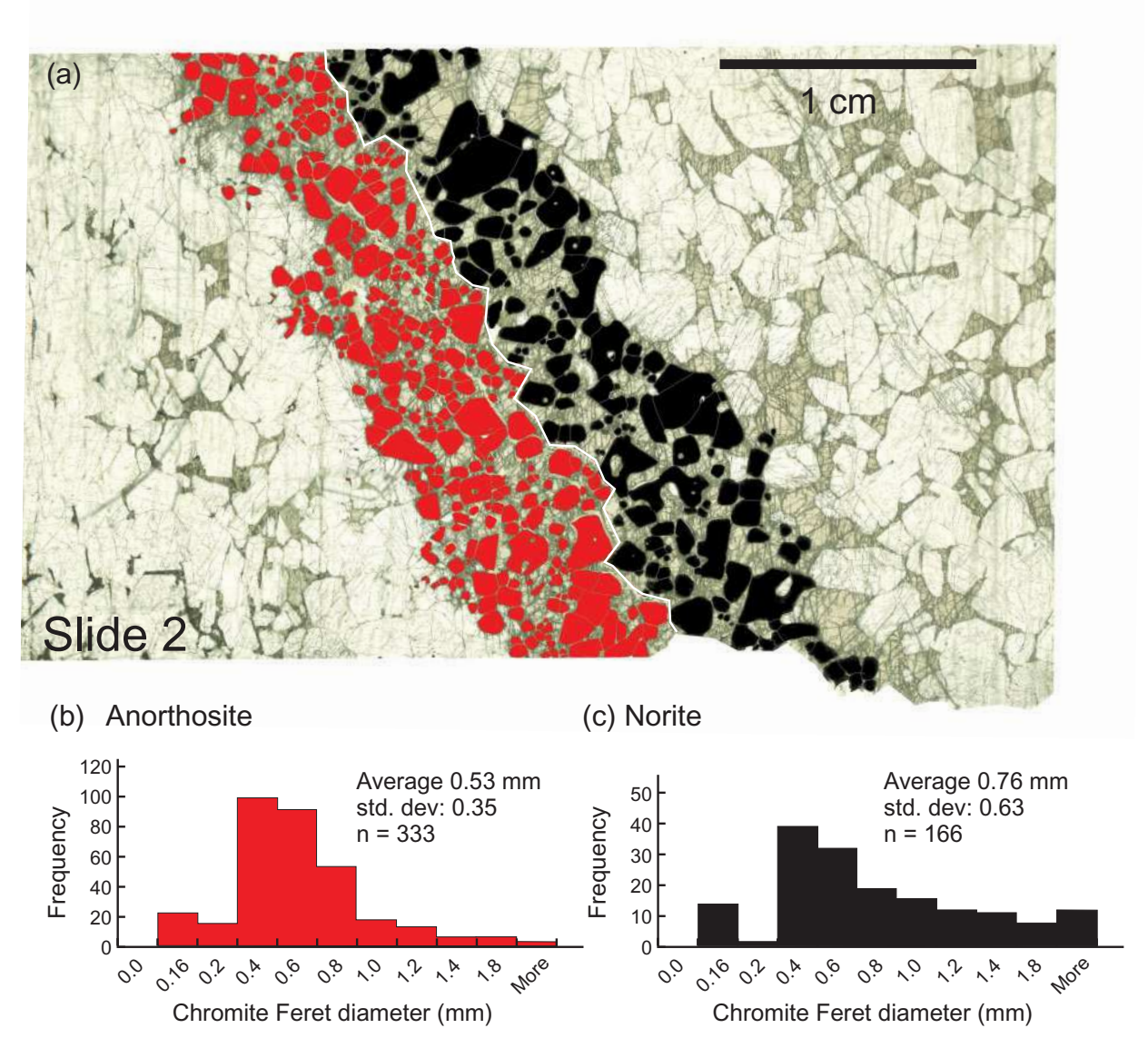


Fig. 10. Crystal size distributions for chromite in the chromitite seam for Slide 2. (a) Outline of chromite grains. The seam was arbitrarily split in half to compare grain sizes next to the anorthosite (red grains) with those on the norite side (black grains). Grain size distributions from each side are shown in the histograms from anorthosite side (b), and norite side (c). Grain sizes are plotted as a function of the Feret diameter, which is the diameter of a circle that has the same area as the grain as measured by ImageJ<sup>®</sup> software. A number of very small chromite grains at the transition between the seam and the anorthosite should be noted.

crystallizing from the injected anorthositic magma to the fractionating, norite-saturated magma already in the chamber.

In the case of the zoned discordant bodies of the Middle Banded series, Meurer et al. (1997) noted that the discordant anorthosites had an average 2 mol% lower An content than the host gabbronorite, similar to the difference seen here between the anorthosite and the norite. Both Meurer et al. and Baker & Boudreau (2019) noted that Cl-bearing, aqueous fluids, initially exsolved from cooler and deeper parts of the crystal pile, will become undersaturated in the more soluble pyroxene components as they move up into hotter parts of the pile such that the fluid becomes saturated in plagioclase alone. Reaction of this fluid with a norite

host results in incongruent dissolution of pyroxene to form olivine by the following generic reaction:

$$\begin{array}{ccc} 2H_2O + Mg_2Si_2O_6 \rightarrow H_4SiO_4 + & Mg_2SiO_4. \\ fluid & opx & fluid & olivine \end{array} \tag{1}$$

With continued fluid inflow, the secondary olivine produced by reaction (1) itself dissolves leaving a residual anorthosite:

$$\begin{array}{lll} 4H^+ + Mg_2SiO_4 \rightarrow H_4SiO_4 + 2Mg^{2+}. \\ & \text{fluid} & \text{olivine} & \text{fluid} & \text{fluid} \end{array} \tag{2}$$

The final reaction sequence is (gabbro)norite (protolith)  $\rightarrow$  troctolite  $\rightarrow$  anorthosite.

It is suggested here that the lithological sequence seen here, norite (protolith)  $\rightarrow$  chromitite  $\rightarrow$  anorthosite,

formed by a similar metasomatic process. The critical difference is that the pyroxene of the Lower Banded series has a higher Cr concentration than the pyroxene higher in the Banded series such that the reaction involves the precipitation of chromite rather than olivine by the incongruent dissolution of a Cr-bearing pyroxene:

With progressive infiltration the chromite itself can dissolve by the generic reaction

$$8HCI + MgCr_2O_4 \rightarrow MgCl_2 + 2CrCl_3 + 4H_2O.$$
 fluid chromite fluid fluid fluid (4)

This is enhanced by the high CI of the fluid, based on the unusually CI-rich nature of the apatite and fluid inclusion evidence. This dissolution is only local, however; the Cr and Mg liberated on the anorthosite side will be carried across the seam and added to the Cr and Mg liberated by the dissolution of orthopyroxene, leading to reprecipitation of the dissolved chromite components. The net effect is that an increasingly chromitite-rich seam that follows the pyroxene dissolution front. Given that chromite contains about two orders of magnitude more  $\text{Cr}_2\text{O}_3$  than does orthopyroxene, it would require a minimum of a 1m equivalent of pyroxene loss to produce a 1cm chromitite seam.

There are two ways by which the addition of an aqueous fluid can produce reverse zoning in plagioclase as seen in the norite. First, the addition of  $\rm H_2O$  leads to a lowering of the plagioclase solid solution loop to lower temperatures (e.g. Yoder & Tilley, 1962). Hydration of a plagioclase–liquid mixture at a constant temperature and pressure will shift both the liquid and the plagioclase to more anorthositic compositions, resulting in a reversely zoned plagioclase.

The second mechanism involves reaction of plagioclase by the incongruent dissolution of plagioclase in silica-poor aqueous fluids (e.g. Adams, 1968; Orville, 1972; Schiffries, 1982):

Eventual crystallization of the hydrated silicate liquid should then crystallize a normally zoned plagioclase unless the hydrated melt is lost or, as is common in the norite, the reverse-zoned plagioclase grains are preserved as chadacrysts in the orthopyroxene oikocrysts.

#### A qualitative model

Volatile-rich fluids invading a partly molten assemblage is a classic physical problem termed 'three-phase flow' (volatile fluid, silicate liquid and a solid matrix) or more broadly 'multi-phase flow'. It is particularly important in

Table 4: Microprobe analysis of amphibole inclusions in chromite from Slide 3

| Analysis:           | 1                           | 2             | 3        | 4        |
|---------------------|-----------------------------|---------------|----------|----------|
| - That yold         | Incl 3-1                    | Incl 3-1      | Incl 3-4 | Incl 3-4 |
| SiO <sub>2</sub>    | $47{\cdot}0\pm0{\cdot}3$    | 47.3          | 46.2     | 47.4     |
| TiO <sub>2</sub>    | $1.78 \pm 0.2$              | 1.62          | 2.01     | 1.68     |
| $Al_2O_3$           | $9.88 \pm 0.1$              | 9.43          | 9.79     | 9.40     |
| $Cr_2O_3$           | $1.76 \pm 0.04$             | 1.78          | 2.03     | 1.61     |
| FeO                 | $5.68 \pm 0.1$              | 5.12          | 5.44     | 5.11     |
| MnO                 | $0.12 \pm 002$              | 0.10          | 0.09     | 0.13     |
| MgO                 | $18.4 \pm 0.1$              | 19⋅0          | 18.8     | 19.6     |
| CaO                 | $10.7 \pm 0.1$              | 10.9          | 10⋅8     | 10.9     |
| Na <sub>2</sub> O   | $2{\cdot}47 \pm 0{\cdot}04$ | 2.64          | 2.89     | 2.17     |
| K <sub>2</sub> O    | $0.22 \pm 0.01$             | 0.20          | 0.13     | 0.11     |
| CI                  | $0.05 \pm 0.02$             | 0.04          | 0.03     | 0.02     |
| F                   | $0.19 \pm 0.2$              | 0.21          | 0.19     | 0.45     |
| H <sub>2</sub> O    | 1.61                        | 1.64          | 1.56     | 1.53     |
| O = F, CI           | -0.09                       | <b>-</b> 0·10 | -0.09    | -0.19    |
| Total               | 99.8                        | 99.8          | 99.8     | 99.9     |
| T site*             |                             |               |          |          |
| Si                  | 6⋅675                       | 6.693         | 6.580    | 6.701    |
| Al                  | 1.325                       | 1.307         | 1.420    | 1.299    |
| C site              |                             |               |          |          |
| Al                  | 0.328                       | 0.268         | 0.223    | 0.269    |
| Ti                  | 0.190                       | 0.173         | 0.216    | 0.178    |
| Cr                  | 0.198                       | 0.199         | 0.229    | 0.179    |
| Fe <sup>3+</sup>    | 0.133                       | 0.129         | 0⋅116    | 0.129    |
| Mg                  | 3.886                       | 4.008         | 3.991    | 4.139    |
| Fe <sup>2+</sup>    | 0.541                       | 0.478         | 0.533    | 0.476    |
| Mn                  | 0.015                       | 0.012         | 0.011    | 0.015    |
| B site              |                             |               |          |          |
| $Mg + Fe^{2+} + Mn$ | 0.289                       | 0.268         | 0.318    | 0.385    |
| Ca                  | 1.634                       | 1.650         | 1.642    | 1.615    |
| Na                  | 0.076                       | 0.082         | 0.040    | 0.000    |
| A site              |                             |               |          |          |
| Ca                  | 0.000                       | 0.000         | 0.000    | 0.032    |
| Na                  | 0.602                       | 0.642         | 0.760    | 0.595    |
| K                   | 0.040                       | 0.036         | 0.023    | 0.019    |
| Sum A               | 0.642                       | 0.678         | 0.783    | 0.646    |
| W site              |                             |               |          |          |
| OH                  | 1.623                       | 1.664         | 1.584    | 1.480    |
| F                   | 0.085                       | 0.094         | 0.087    | 0.202    |
| CI                  | 0.012                       | 0.010         | 0.007    | 0.005    |
| 0                   | 0.280                       | 0.232         | 0.323    | 0.313    |

<sup>\*</sup>Site population and pressure estimates using AMFORM spreadsheet (Ridolfi et al., 2018).

understanding degassing in more traditional magmatic fluid transport in granite systems (see Lamy-Chappuis et al., 2020, for a recent review), but the phenomenon is common to the degassing of any crystal-rich system. A complicating factor involves those cases in which the invading fluid is reactive (e.g. Parmigiani et al., 2011), as is suggested for the case here. Although buoyant fluids have a propensity to rise vertically, the inherently anisotropic nature of layered intrusions and the common observation of layer-conformable pegmatites suggests that the fluids can be readily induced to move laterally when confronted with porosity-permeability barriers.

A qualitative model is presented below to explain the development of a chromitite seam by the infiltration of a reactive fluid into a partly molten norite that is not yet saturated in fluid or clinopyroxene. Following Meurer et al. (1997), fluids generated by crystallization of interstitial liquids deeper in the crystal pile rise into hotter part of the crystal pile. As they do so, they become

undersaturated in pyroxene (and chromite) relative to the more insoluble plagioclase. The infiltration of this plagioclase-saturated but pyroxene- and chromiteundersaturated fluid will produce a series of mineral zones as it reacts with a partly molten, fluidundersaturated, noritic mush as illustrated in Fig. 11. Owing to inherent inhomogeneity in the porosity and permeability of the layered host rocks, the fluid moves laterally as well as upward; this can be favored if there is any dip to the igneous layering. (Although the fluid is assumed to be moving horizontally in Fig. 11 to produce the observed vertical discordant layering, there is no reason why it cannot happen with vertical fluid flow to produce a horizontal sequence of rocks broadly concordant with the regional igneous layering.) Finally, except at the reaction fronts, it is assumed that volatile fluid, silicate liquid and mineral assemblages are all in local equilibrium.

The initial introduction of the fluid encounters the fluid-undersaturated noritic mush (Fig. 11a). Initially, this fluid will redissolve in the interstitial silicate liquids, induced a modest remelting of the plagioclase and pyroxene. This modest remelting is based on the observation that the orthopyroxene oikocrysts have coarse cores, interpreted to be residual unmelted primocrysts. This modest flux melting event apparently did not induce chromite saturation by incongruent melting of the original plagioclase + orthopyroxene assemblage (at least that which may have been preserved and not reincorporated into pyroxene on eventual solidification). The partial melting of the plagioclase also results in a reversely zoned plagioclase.

If the amount of interstitial liquid is minor and near fluid saturation, then it would take very little fluid addition to drive the interstitial liquid to fluid saturation. The result is that a fluid saturation front develops between the original norite (shown on the right of Fig. 11a) and a fluid-saturated norite with some additional hydration melt (shown on the left) that moves to the right over time. Furthermore, once the pyroxene-undersaturated fluid equilibrates with the solid + liquid assemblage (by dissolving pyroxene), the plagioclase + pyroxene-saturated fluid moves through the rest of the vapor-saturated mush without effect until it reaches the vapor saturation front. Equilibration of the silicate liquid with the fluid also enriches the liquid in CI in addition to presumed fluid components  $H_2O$  and  $CO_2$ .

Although melting stops, the pyroxene continues to dissolve as the pyroxene-undersaturated fluid continues to infiltrate the norite mush, the pyroxene being dissolved along a sharp reaction front (Fig. 11b). At this 'pyroxene-out' front, the dissolution of pyroxene increases the local concentration of the pyroxene components in the fluid, including the relatively insoluble Mg and Cr, and this, in turn, drives the solution to precipitate chrome spinel. Once the pyroxene is fully dissolved, chromite precipitation ceases, and further infiltration of the plagioclase-saturated fluid redissolves the chromite. The dissolved Cr moves across

**Table 5:** Biotite and apatite inclusions in chromite electron microprobe analyses

| Analysis:                      | 1                           | 2               | 3     |
|--------------------------------|-----------------------------|-----------------|-------|
| •                              | Inc 4                       | Inc 1           | Inc 1 |
|                                | Impure Bt                   | Ap 1            | Ap 2  |
| SiO <sub>2</sub>               | 38·87 ± 0·3                 | 0.25            | 0.18  |
| TiO <sub>2</sub>               | $3.31 \pm 0.2$              | _               | _     |
| $Al_2O_3$                      | $17{\cdot}43 \pm 0{\cdot}3$ | _               | _     |
| FeO                            | $4{\cdot}49\pm0{\cdot}2$    | _               | _     |
| MnO                            | $0.07 \pm 0.03$             | _               | _     |
| MgO                            | $26.98 \pm 0.2$             | _               | _     |
| CaO                            | $0.69 \pm 0.05$             | $53.5 \pm 0.3$  | 53.7  |
| Na <sub>2</sub> O              | $0{\cdot}45 \pm 0{\cdot}03$ | n.d.            | n.d.  |
| K <sub>2</sub> O               | $3{\cdot}27\pm0{\cdot}2$    | _               | _     |
| $P_2O_5$                       | _                           | $40.8 \pm 0.3$  | 40⋅8  |
| La <sub>2</sub> O <sub>3</sub> | _                           | $0.07 \pm 0.03$ | 0.08  |
| Ce <sub>2</sub> O <sub>3</sub> | _                           | $0.15 \pm 0.03$ | 0.27  |
| $Nd_2O_3$                      | _                           | $0.07 \pm 0.3$  | 0.13  |
| CI                             | $0.05 \pm 0.03$             | $3.23\pm0.25$   | 3.88  |
| F                              | $0.58\pm0.3$                | $0.08 \pm 0.3$  | 0.30  |
| 0*                             | 3.81                        | 0.85            | 0.60  |
| O = F, CI                      | -0.26                       | –0.76           | –1⋅00 |
| Total                          | 99.7                        | 98.3            | 99.0  |
| X(CI)                          | 0.00                        | 0.48            | 0.57  |
| <i>X</i> (F)                   | 0.07                        | 0.02            | 0.08  |
| <i>X</i> (OH)                  | 0.93                        | 0.50            | 0.35  |
| Si + AI                        | 3.840                       | _               |       |
| Ti + Fe + Mn + Mg              | 3.399                       | _               | _     |
| Ca + Na + K                    | 0.422                       | _               | _     |

<sup>\*</sup>H<sub>2</sub>O from site vacancy.

the seam only to be re-precipitated as chromite where pyroxene is actively dissolving, as noted above. The preference of small chromite grains to occur in the anorthosite side of the seam is consistent with this redissolution of chromite on the upstream side of the seam. The net effect is the development of two sharp reaction fronts, one the 'chromite out' front on the anorthosite side of the seam and a 'pyroxene-out, chromite-in' front on the norite side of the seam where pyroxene is dissolving and chromite precipitating. Both fronts and the chromitite seam they define move in the direction of fluid flow over time, and the size of the seam also increases as it contains all the Cr liberated from the formation of the replacement anorthosite.

Owing to the low solubility of Al in the fluid phase, the Al component of chromite is supplied, in part, by the local reaction with the plagioclase. This dissolution of plagioclase liberates Ca, Na, and Si, the latter two in particular acting as fluxing agents that enhance local remelting. Samples of this hydrous, alkali-rich liquid are preserved as the (now crystallized) amphibole- and biotite-containing polyphase inclusions that occur in the chromite. This reaction with plagioclase will be minor early in the development of the chromitite seam when the amount of chromite is minor, but becomes more pronounced as more and more chromite forms at the advancing front, as shown schematically as the chromitite seam moves left and becomes richer in chromite in Fig. 11b and c. Eventually, as the seam continues to migrate and become more chromite-rich, enough plagioclase is reacted-remelted such that only

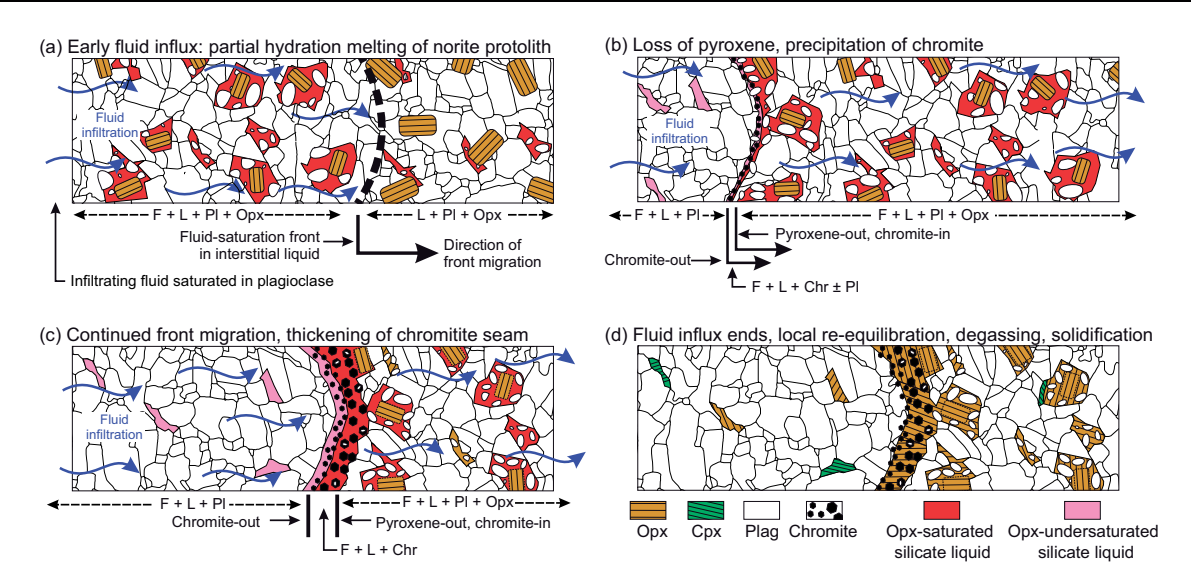


Fig. 11. Illustration of the development of a replacement anorthosite and associated chromitite seam as a fluid saturated in plagioclase alone reacts with a partially molten norite, in part schematic. F, fluid; L, silicate liquid; Pl, plagioclase; Opx, orthopyroxene; Cpx, clinopyroxene; Chr, chromite. (a) The early infiltration of fluid from the left into an initially partly molten, fluid-undersaturated noritic assemblage (shown on right) induces hydration melting until the interstitial liquid (shown in red) becomes saturated. (b) Continued fluid infiltration into the fluid-saturated norite produces a moving chromitite seam that moves to the right with time. Within the anorthosite, the fluid continues to deplete the interstitial liquid of pyroxene components, leaving the interstitial liquid far from saturation in pyroxene (shown in pink). (c) Same as for (b), but the chromitite has moved further right and is thicker, having collected all the Cr lost to the developing anorthosite. (d) Once infiltration stops, pyroxene components in the interstitial liquid diffuse from the pyroxene-saturated interstitial liquid across the seam to the interstitial liquid poor in pyroxene components on the anorthosite side. (See text for additional details.)

that plagioclase trapped as rounded 'accidental' inclusions in chromite remains in the seam. The eventual passing chromitite seam leaves a lower An content plagioclase in the anorthosite.

Once fluid infiltration stops the advancement of the seam also stops, but there are a number of phenomena that continue to modify the system (Fig. 11d). The seam separates pyroxene-saturated interstitial liquid in the norite from the interstitial liquid in the anorthosite that has lost much of its pyroxene component to the fluid. In addition, the melting-dissolution of plagioclase to supply the Al spinel component in the chromite leaves a local high concentration of Na, Si and Ca in the seam itself. Pyroxene components in the liquid diffuse into the seam from the norite side to cause the precipitation of the oikocrystic orthopyroxene in the seam while the simultaneous outward diffusion of the alkalis away from the seam leads to the formation of the lower An plagioclase just outside the seam.

Boudreau (2010) has noted that surface free energy of chromite, and hence chromite solubility, is a function of the types of minerals in contact with chromite. It was suggested that a chromite–chromite contact has a lower overall free energy than a plagioclase–chromite contact, with the former having a lower solution solubility than the latter. Because chromite was actively precipitating at the norite side of the seam, the chromite here is more likely to have chromite–chromite contacts. These grains will continue to grow by annealing once the reactive fluid infiltration event stops, leading to a preference for

the large agglomerated grains to form on the norite side of the seam.

As the system continues to cool, any residual interstitial silicate liquid will crystallize and degas, the amount of fluid generated being small relative to the mass flux that drove the initial metasomatic reactions. Passive degassing of the interstitial liquid leads to a lower P(H<sub>2</sub>O) while the rocks are still hot such that amphibole and biotite never become stable minerals that could crystallize from the residual silicate liquid. The exceptions are the hydrous melt inclusions in the chromite that did not lose their volatile components. The degassed interstitial liquid on the norite side crystallizes the large orthopyroxene oikocrysts, which grow as overgrowths on residual pyroxene primocrysts grains, enclosing plagioclase and preserving the reverse zoning present in the plagioclase. In the anorthocrystallization of the plagioclase-saturated interstitial liquid crystalizes more plagioclase to produce a normally zoned plagioclase, followed by the later cotectic crystallization of orthopyroxene and clinopyroxene as an interstitial space filler and incorporating Cr not transported earlier to the chromitite seam. Finally, late Mg-Fe exchange between the chromite and pyroxene continues during subsolidus cooling leading to Fe-enrichment in the chromite and Mg-enrichment in the pyroxene.

# Mineral solubility considerations

Any quantitative model for the formation of chromitite seams by infiltration-reaction requires some

knowledge of mineral solubility in the temperaturepressure range of interest. Estimates of the crystallization temperature-pressure ranges for large layered intrusions such as the Stillwater and Bushveld complexes are ~1300-900 °C at upper crustal pressures of 0.2-0.4 GPa. Unfortunately, this is a region in which mineral solubility experiments are mostly absent (Fig. 12). Most experimental work at upper crustal pressures is focused on the temperature range appropriate for granites (T < 900 °C). Higher-temperature experiments are generally restricted to pressure appropriate for lower crustal-upper mantle conditions. Given that the Stillwater fluids could be interacting with a mush that is near or just below its liquidus, one needs to extrapolate these experiments to higher temperatures where other aqueous species can become increasingly important but have been poorly explored.

For example, at lower temperatures (<700 °C), dissolved silica is typically present as a hydrated species, generally denoted as H<sub>4</sub>SiO<sub>4</sub>, SiO<sub>2</sub>·2H<sub>2</sub>O, or simply SiO<sub>2,aq</sub> as used here. However, experimental work by Newton & Manning (2000, 2016) found that that modest amounts of NaCl in a hydrous fluid ( $X_{NaCl} \cong 0.1$ ) can cause a roughly 50% increase in SiO2 solubility compared with NaCl-absent aqueous fluids at 700°C and 0.2 GPa. They showed that this effect diminishes with increasing pressure (presumably because of increasing CI-Na complexing in the fluid) but the effect of increasing temperature above 700°C is unknown. These experiments show the potential importance of CI-Na dissociation in enhancing silica solubility at high temperatures that is not significant at lower temperatures and is not typically considered in current thermodynamic databases.

Furthermore, for many minerals, including eskolaite (Cr<sub>2</sub>O<sub>3</sub>), solubility can decrease as temperature rises. Experimental work by Watenphul et al. (2014) in aqueous HCl solutions between 400 and 700 °C and 0.2 and 0.9 GPa showed that the Cr solubility decreases with temperature and increases with pressure. Similar to the Newton & Manning (2000) silica solubility study, Watenphul et al. attributed this retrograde solubility behavior to the T, P dependence for HCl<sup>0</sup> complexing and its effect on Cl<sup>-</sup> activity. The experimental values of the Watenphul et al. study closest to Stillwater pressures of 0.2-0.3 GPa (Labotka & Kath 2001) are 0.480 GPa and 700 °C, for which the Cr concentration in the fluid is about 4000 ppm. This may be compared with the Cr concentration of natural basalt and boninitic liquids, which contain 20-700 ppm Cr (Gale et al., 2013). Although Watenphul et al. noted negligible Cr solubility in Na<sub>2</sub>CO<sub>3</sub>-H<sub>2</sub>O and Na<sub>2</sub>Si<sub>3</sub>O<sub>7</sub>-H<sub>2</sub>O solutions, the effect of a mixed Na-Cl-C-O-H fluid remains unexplored.

Huang et al. (2019) derived thermodynamic parameters for a number of Cr–Cl–OH species from the Watenphul et al. (2014) study. In contrast to the study by Watenphul et al., who mainly considered trivalent Cr, the analysis by Huang et al. suggests that Cr is mainly dissolved as a divalent cation in the neutral complex

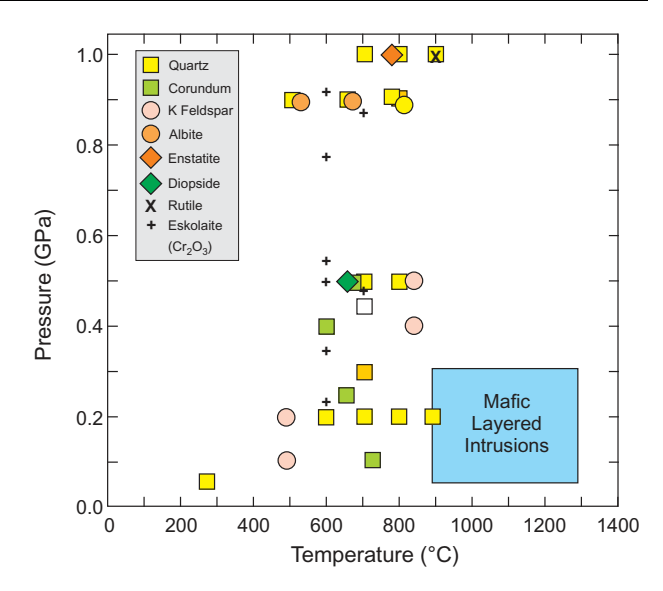


Fig. 12. Temperature–pressure range of some high-temperature mineral solubility experiments in C–O–H–Cl fluids applicable to mafic–ultramafic layered intrusions. Large box shows the crystallization range of mafic and ultramafic layered intrusions. Experimental data from Weill & Fyfe (1964), Anderson & Burnham (1967, 1983), Novgorodov (1975, 1977), Fournier and Rowe (1977), Walther & Orville (1983), Manning (1994), Newton & Manning (2000, 2016), Shmulovich *et al.* (2006a, 2006b), Antignano & Manning (2008), and Watenphul *et al.* (2014).

CrCI(OH)<sup>0</sup> in CI-rich, high-temperature solutions, and that Cr solubility increases with both increasing CI concentrations, decreasing temperatures, and decreasing f(O<sub>2</sub>). However, it is again noted that these calculated values are based on experiments that are at least 400–500 °C below a Stillwater crystal pile temperature that could be in excess of 1100 °C (Helz, 1995). Indeed, their calculated dissociation constants for eskolaite overestimate the experimental Cr solubility at 500 °C and underestimate it at 700 °C at upper crustal pressures. Experimental work in the range appropriate to maficultramafic layered intrusion is warranted.

#### **Activity diagram analysis**

Given the solubility caveats noted above, the development of the mineral zones is consistent with fluid–mineral activity diagram considerations. Shown in Fig. 13 are two activity diagrams for  $\log(a_{\rm Mg^{2+}}/a_{\rm H^+}^2)$  plotted against the log of the activity of aqueous silica,  $a_{\rm SiO_{2,aq}}$ , showing the expansion of the magnesiochromite field with increasing concentration of dissolved Cr. Equilibrium relationships are calculated using the CHNOSZ software package v. 1.3.2 (Dick, 2019) developed for the R software environment (R Core Team, 2019). The program is an extensive upgrade of the classic SUPCRT92 thermodynamic calculation program (Johnson *et al.*, 1992) and has an interactive text-based interface and the ability to produce quality graphical output.

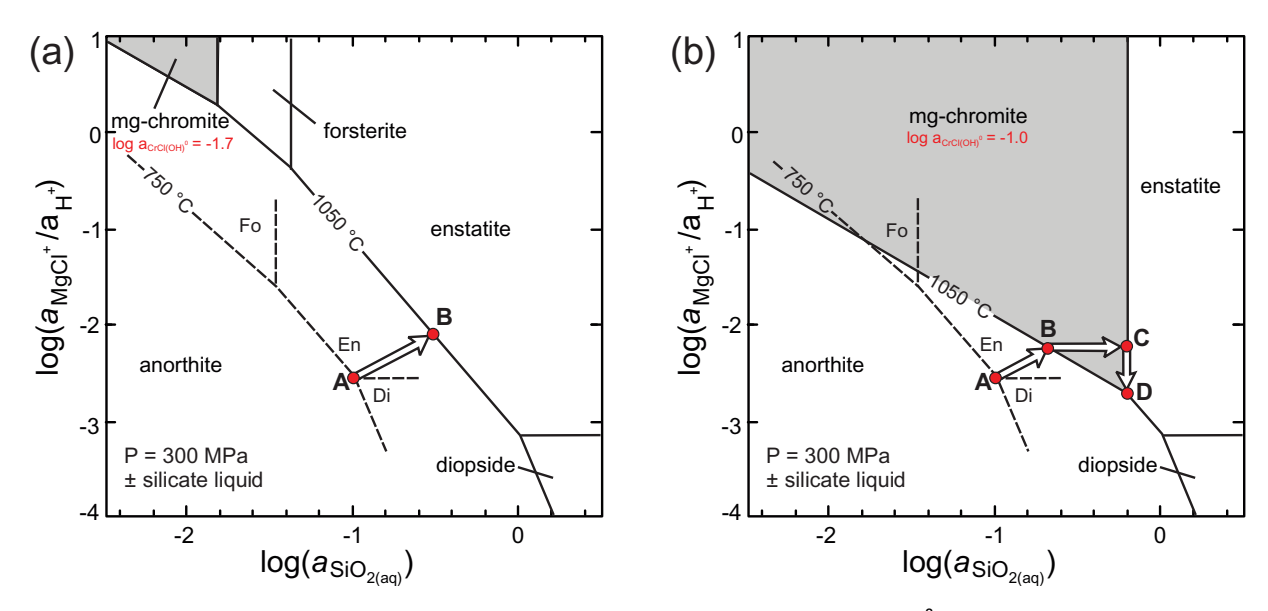


Fig. 13. Activity–concentration diagram of the log of the aqueous fluid activity ratio,  $a_{Mg^{2+}}/a_{H^+}^2$ , against the log of the activity of aqueous silica,  $a_{SiO_{2,aq}}$ , illustrating the expansion of the magnesiochromite field with increasing activity of  $CrCl(OH)^0$  at 950 °C and 300 GPa. Also shown are the phase boundaries at 650 °C in a Cr-poor system (dashed lines). Plot (a) illustrates that a fluid in equilibrium with a Cr-poor system anorthite + enstatite + diopside at 650 °C (point 'A') will be saturated in plagioclase alone at 950 °C and will react until it equilibrates at point 'B' without precipitation of chromite. Plot (b) shows the same fluid reacting with a system with a higher activity of  $CrCl(OH)^0$  and expanded chromite phase field, where reaction leads to chromite precipitation. All continuous line mineral boundaries are balanced on  $H_2O$  in the formation from solution reactions at  $f(O_2) = FMO$ . Other mineral and solution activities are listed in the 'R' script in the Supplementary Data. (See text for additional discussion.)

The lack of amphiboles and biotite (excluding those in chromite inclusions) implies that reactions are occurring under T-P conditions that are above the stability of these mineral and are broadly similar to granulite-facies conditions (>700°C) at Stillwater crystallization pressures. For the diagrams shown in Fig. 13, all reactions are balanced on H<sub>2</sub>O in the mineral formation reactions at 750 °C (dashed lines) and 1050 °C (continuous lines) and 0.3 GPa. Activities for the solid phases are based on mineral compositions reported here and activities calculated with the program PELE (Boudreau, 1999b). Thermodynamic data for magnesiochromite (MgCr<sub>2</sub>O<sub>4</sub>; Klemme et al., 2000) and a number of chloride and other Cr aqueous species (Huang et al., 2019) were added to the CHNOSZ database. Following the thermodynamic analysis of Huang et al. noted above, it is assumed that Cr is mainly dissolved as a divalent cation in the neutral species CrCl(OH)<sup>0</sup> at the temperatures used here. The R scripts used to produce the diagrams are included in the Supplementary Data.

Although not generally considered in activity diagrams at lower temperatures, an interstitial silicate liquid is a likely additional phase universally present at these temperatures. That is, the assemblages shown in Fig. 13 can include a silicate liquid in addition to both a fluid and the stable minerals shown, subject to the silicate liquid being constrained to have a composition in equilibrium with the local fluid–mineral assemblage.

In Fig. 13a, at the arbitrary lower temperature of  $750\,^{\circ}$ C, a Cr-poor fluid at point A will be saturated in a typical Lower Banded series assemblage of anorthite +

enstatite + diopside. Heating of this fluid to  $1050\,^{\circ}\mathrm{C}$  results in the fluid being in the anorthite-alone field. Infiltration of this heated fluid into a partially molten norite would result in some enstatite dissolving as the fluid re-equilibrates with the hotter assemblage, increasing both  $\mathrm{MgCl_2}$  and  $\mathrm{SiO_{2,aq}}$  as the fluid moves to point B. In a Cr-poor system, this reaction does not lead to the precipitation of chromite and the zoned rock sequence is simply anorthosite—norite.

In the more Cr-rich system shown in Fig. 13b, the liberation of Cr from the dissolution of Cr-bearing pyroxene leads to both an increase in the Cr concentration of the fluid and an increase in the chromite field that expands as a wedge between the anorthite and enstatite fields. This results in chromite precipitating at point B prior to the fluid becoming saturated in pyroxene. Dissolution of both plagioclase and pyroxene and the precipitation of chromite leads the solution to mainly increase its silica concentration and chromite being the only mineral phase present (± silicate liquid) from points B to C. The fluid becomes saturated in pyroxene at point C. The observed assemblage, chromite + orthopyroxene, suggests that the final assemblage in the main part of the seam is at point C, except at the margins of the seam on the anorthosite side, where the stable assemblage is at point B, and at the margins of the seam on the norite side where the assemblage is at point D.

# A simple numerical model

A simple quantitative numerical model illustrates how a chromitite seam can form by reactive fluid infiltration

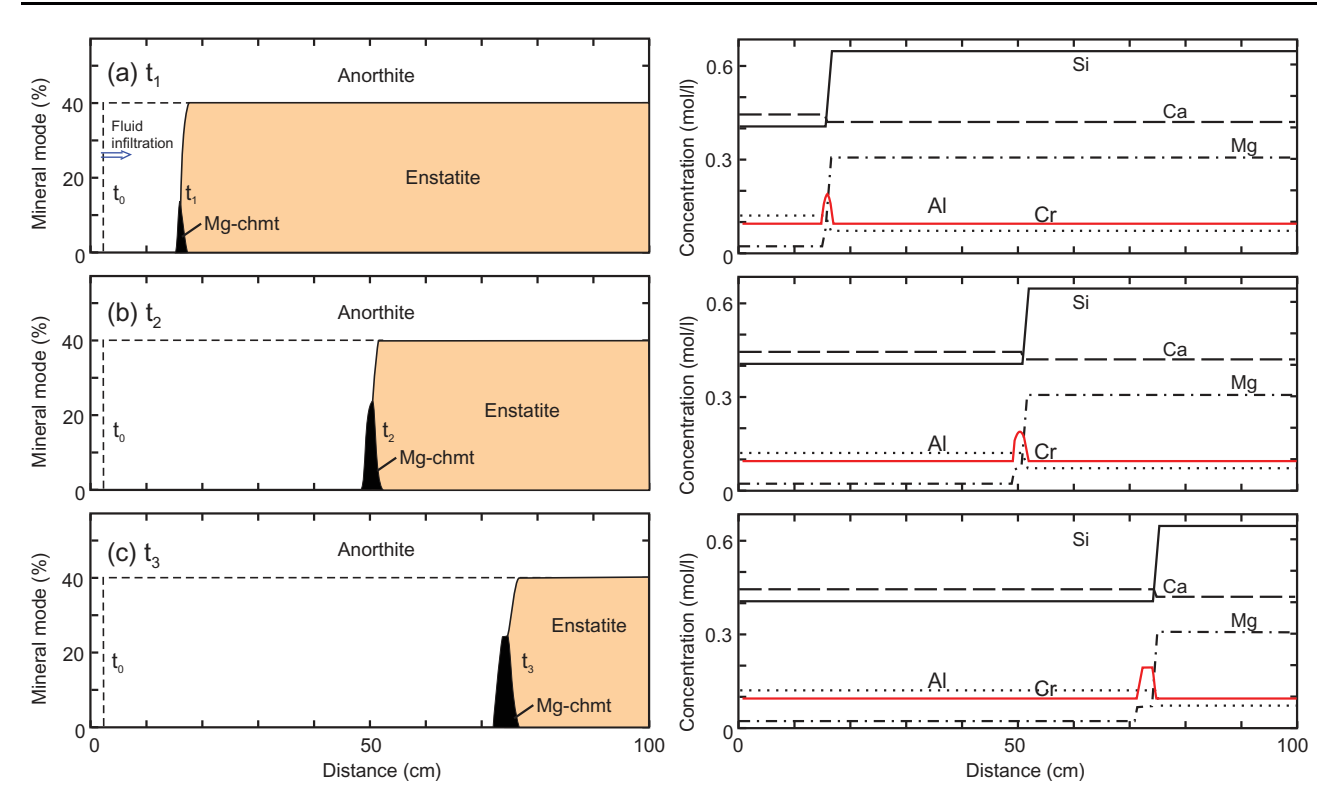


Fig. 14. Numerical model of chromitite seam formation (Case 1) by reactive fluid infiltration. The three pairs of figures (a)–(c) show the evolution of the system at three arbitrary times  $t_1$ ,  $t_2$ ,  $t_3$ , respectively, after the start of the infiltration at  $t_0$ . Figures on the left are modal variations, those on the right are solution concentrations. Original enstatite mode is shown as the dashed line at time  $t_0$  and magnesiochromite mode is shown by the black field in the mode plots. Fluid is infiltrating from the left. (See text for additional discussion.)

into a norite assemblage. The model considers only three endmember minerals (anorthite, enstatite and magnesiochromite) and a fluid. For simplicity, we ignore the possibility of silicate liquid also being present as it is a passive actor that simply remains in equilibrium with the local assemblage. Mineral solubility is typically assumed to be a function of concentration of specific solution species; for example,

$$MgSiO_3 + 2H^+ = Mg^{+2} + H_2SiO_4.$$
opx fluid fluid fluid (6)

However, to dissolve or precipitate minerals in abundance to significantly change the bulk composition of a rock, one needs ideally to know all the dominant solution species, which for the case of Mg and especially  $SiO_2$  can include Cl complexes at higher temperatures. In the model developed here, mineral solubility is simply assumed to be a function of total solution concentration of the component elements expressed as simple single cation oxides; for example,

$$\begin{aligned} &\text{MgSiO}_3 = \text{MgO} + \text{SiO}_2. \\ &\text{enstatite} & &\text{fluid} & &\text{fluid} \end{aligned} \tag{7}$$

For which one can define the solubility constant

$$K_{\rm En} = C_{\rm MgO}.C_{\rm SiO_2}$$
 (8)

where the concentration, C, of the subscripted

component is the total dissolved concentration (mol l<sup>-1</sup>) of the element (Mg, Si, etc.) expressed as an oxide. For magnesiochromite and anorthite, the solubility constants are defined as follows:

$$K_{\text{Mg-chmt}} = C_{\text{MgO}} \cdot (C_{\text{CrO}_{15}})^2 \tag{9}$$

$$K_{An} = C_{CaO}.(C_{AlO_{15}})^2.(C_{SiO_2})^2.$$
 (10)

The orthopyroxene is also assumed to contain 2 mol% CrO<sub>1.5</sub>. The program CHROMITE\_SEAM models the infiltration of an anorthite-saturated fluid into an anorthite + Cr-bearing enstatite assemblage (norite). The program is included as part of the Supplementary Data.

Examples of the range of phenomenon that can occur are shown as four cases in Figs 14 and 15. In these figures, a volatile fluid (saturated in anorthite alone) infiltrates into an assemblage composed of 50 % anorthite + 40 % Cr-bearing enstatite. The fluid moves from left to right. Time steps are arbitrary, as the governing parameter is the rate of fluid fluxing through the assemblage, which by itself (and ignoring diffusion) does not affect the precipitation–dissolution mechanism. Parameters for the four cases are listed in Table 6. The minerals are assumed to dissolve congruently except for enstatite → chromite, as noted above. The infiltration results in all cases in a loss of enstatite at a sharp front, but chromite behavior can be more variable as noted in the discussion of the four cases below. The

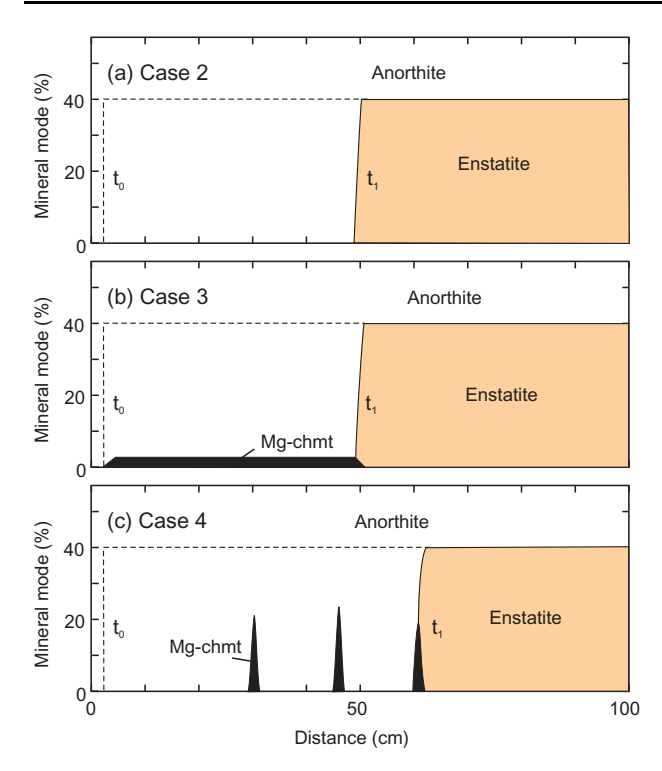


**Fig. 15.** Numerical models showing the mineral mode changes for Cases 2–4 at some arbitrary time  $t_1$  after the start of the simulation at  $t_0$ . As for the previous figure, the dashed lines show the initial mode enstatite at time  $t_0$  and fluid infiltration is from the left. (a) Case 2. Resorption of enstatite does not result in chromite saturation anywhere. (b) Case 3. Chromite precipitates as enstatite dissolves, but it is too insoluble to be resorbed once the enstatite-out front passes, resulting in an anorthosite with minor disseminated chromite. (c) Case 4. Chromite solubility is lower where chromite-chromite contacts predominate over chromite—anorthite contacts owing to surface energy considerations. The result is a series of thin chromitite seams left behind in the anorthite after the enstatite-out front has passed, as well as the chromitite developing at the enstatite-out front. (See text for additional discussion.)

model chromite is pure endmember magnesiochromite, which composes only about half of the observed chromite composition. Thus, we assume that the real amount of chromite precipitation would be about twice the model modes shown.

# Case 1. Chromite precipitation at the enstatite-out front

This case is illustrated in the three pairs of plots at three dimensionless times shown in Fig. 14, the plots on the left showing thse change in mineral mode and those on the right the solution concentrations. Fluid inflow from the left leads to a local increase in the solution concentration of Mg, Si and Cr liberated from the dissolution of enstatite. The increase in Si in the fluid leads to a modest precipitation of plagioclase, but overall there is a net loss of solids owing to the loss of enstatite. Where enstatite is actively dissolving, the increase in dissolved Mg and Cr in the fluid leads to chromite precipitation. However, once enstatite is gone, the chromite itself

redissolves from the continued influx of Crundersaturated fluid, to produce a chromite-saturated fluid, only to be reprecipitated as soon as these Cr-rich solutions again are enriched in Mg at the enstatite-out front. This is seen in the sharp peak in Cr concentration in the fluid in the seam; it increases as the fluid dissolves some chromite on the anorthosite side, only to fall again when chromite reprecipitates where the enstatite is dissolving. The net effect is that the chromite precipitation front and the enstatite-out front move at the same speed. Furthermore, the amount of chromite in the seam increases as the fronts move to the right as essentially all the Cr lost from the dissolved enstatite is concentrated in the chromitite seam.

The total fluid flux required to produce the seam and roughly  $0.5\,\mathrm{m}$  of anorthosite shown in Fig. 14b is  $\sim 1.2\,\mathrm{l\,cm^{-2}}$ . Although this is dependent on the starting parameters, in general, one might expect flux rates of the order of a few  $1\,\mathrm{cm^{-2}}$  to produce a meter-sized replacement anorthosite and associated chromitite seam. Given that one has about  $2\,\mathrm{km}$  of degassing interstitial liquid beneath the J-M Reef (plus any fluid released by dehydration of the underlying metamorphic aureole) and that this fluid can be concentrated by channeling or fluid focused flow, the generation of the required volumes of fluid to form the anorthite body and its associated chromitites is not unreasonable.

# Case 2. No chromite precipitation

For relatively high chromite solubility constants or low initial solution concentrations of Cr, the Cr and Mg liberated during the dissolution of pyroxene is not enough to drive the fluid to chromite saturation, and one simply has a sharp front separating the anorthosite from the norite that advances in the direction of fluid flow over time (Fig. 15a). This would be the case for those replacement anorthosites seen higher in the Banded series, where replacement of Cr-poor norite with anorthosite does not liberate enough Cr to precipitate chromite. Again, once the fluid equilibrates with enstatite at the enstatite-out front, it moves through the norite without further effect.

# Case 3. Strongly insoluble chromite

For low values of  $K_{\rm Mg-chmt}$ , Cr has a low solubility and dissolution of pyroxene results in the precipitation of chromite that later is left behind as part of the anorthosite assemblage (Fig. 15b). In this case the pyroxene-out front moves faster than the chromite-out front. Although rare in the Stillwater Complex, minor disseminated chromite in anorthosite has been noted in drill core from OB-I. Chromitiferous anorthosite is also found in the Rum intrusion (O'Driscoll *et al.*, 2010).

#### Case 4. Multiple chromitite seams

Chromite precipitating as in Case 1 can be strongly affected by surface free energy considerations as noted above such that surface free energy, and hence mineral

Table 6: Parameters used in numerical modeling

|  | Case 1               | Case 2               | Case 3               | Case 4  |
|--|----------------------|----------------------|----------------------|---|
| Initial infiltrating solution concentration (mol l <sup>-1</sup> ) |                      |                      |                      |   |
| SiO <sub>2</sub>   | 0.4                  | 0.4                  | 0.4                  | 0.4   |
| AIO <sub>1.5</sub> *   | 0.118                | 0.118                | 0.118                | 0.118   |
| MgÓ  | 0.03                 | 0.03                 | 0.03                 | 0.03  |
| CaO  | 0.45                 | 0.45                 | 0.45                 | 0.45  |
| CrO <sub>1.5</sub>   | 0.1                  | 0.1                  | 0.01                 | 0.1   |
| Dissolution constants  |                      |                      |                      |   |
| $K_{An}$   | $1.0 \times 10^{-3}$ | $1.0 \times 10^{-3}$ | $1.0 \times 10^{-3}$ | $1.0 \times 10^{-3}$                                |
| κ <sub>En</sub>  | $2.0 \times 10^{-1}$ | $2.0 \times 10^{-1}$ | $2.0 \times 10^{-1}$ | $2.0 \times 10^{-1}$                                |
| $K_{\text{Mg-chmt}}^{\text{Lii}}$                                  | $3.2 \times 10^{-3}$ | $3.0 \times 10^{-2}$ | $3.1 \times 10^{-6}$ | $3.2 \times 10^{-3} (3.2 \times 10^{-4})^{\dagger}$ |
| Initial Cr in enstatite (mole fraction)                            |                      |                      |                      |   |
| $X^{Cr}(En)$   | 0.02                 | 0.02                 | 0.02                 | 0.02  |

Bold type denotes those parameters changed from Case 1.

solubility, is a function of the minerals in contact with chromite. A chromite–chromite contact has a lower overall free energy than a plagioclase–chromite contact, with the former having a lower solution solubility than the latter; for example,  $K_{\rm Mg-chmt}$  would be lower for a region rich in chromite–chromite contact compared with a region where chromite–anorthite contacts predominate. These kinds of surface energy considerations can be important to the development of modal layering (Boudreau, 2010, and references therein).

This is shown as Case 4 in Fig. 15c; here it is arbitrarily assumed that  $K_{\rm Mg-chmt}$  is decreased by an order of magnitude once the modal amount of chromite exceeds 0.25 volume fraction and chromite–chromite contacts start to form. In this case, chromitite seams develop where enstatite is actively dissolving, but once the mode exceeds 25 mol% chromite becomes relatively insoluble and the seam does not significantly dissolve once the enstatite is completely removed. Instead, the seam is left behind and a new seam begins to form at the enstatite-out front, until it too exceeds 25 mol% chromite and the cycle is repeated. The similarity of the results shown here, when scaled up, can be compared with the spectacular chromitite–anorthosite layering at the classic Dwars River outcrop in the Bushveld Complex.

In general, the modeling suggests that the development of discrete seams occurs most readily when solution concentrations are near chromite saturation. For a fluid strongly undersaturated in Cr, chromite either never becomes saturated in chromite or chromite saturation is ephemeral and is eventually removed by the infiltrating fluid. If the Cr concentration of the solution is too high or solubility constants are too low, chromite precipitates as part of the residual assemblage and very little may move once it precipitates.

The numerical results can be applied to other systems as well. For example, chromitite seams are found at the margins of replacement dunite hosted by pyroxenite in the Ultramafic series (Raedeke & McCallum, 1984). In this case, a silica-poor fluid reacts with Crbearing pyroxenite to produce olivine and again precipitate chromite at the pyroxene dissolution front.

# Implication for sulfide-chromitite associations

Although not seen here, PGE-bearing sulfides are commonly associated with chromitites. The abundant PGE-sulfides seen in the discordant anorthosite of this study suggest that the fluids do have a significant ore component. As noted above, Cr is dissolved largely as a divalent ion in the CrCl(OH)<sup>0</sup> complex at the temperatures and pressures of interest here (Huang *et al.*, 2019), whereas Cr is trivalent in chromite. Thus, precipitation of chromite would require an oxidation step in the precipitation reaction. This can result in the coprecipitation of sulfide via redox reactions involving solution species including FeCl<sub>2</sub>, SO<sub>2</sub>, and H<sub>2</sub>S. An example reaction using neutral solution species to produce the co-precipitation of ferrochromite component of chromite and pyrrhotite is as follows:

As for chromite, one could envision a sulfide front moving with the developing chromitite seam, the above reaction going to the right and precipitating with chromite but the reaction reversed during the Cr reduction involved in chromite dissolution.

# **CONCLUSIONS**

Zoned anorthositic replacement bodies are not uncommon in the Banded series of the Stillwater Complex. The data presented here are all broadly consistent with a metasomatic, chromatographic model of chromite precipitation at a reaction front as a norite protolith reacts with a Cl-rich volatile fluid, which became saturated in plagioclase alone as it rose into hotter parts of the crystal pile. As this reactive fluid moved through a partially molten norite assemblage, chromite is precipitated during the incongruent dissolution of Cr-bearing orthopyroxene. Continued fluid influx led to redissolution and reprecipitation of chromite (± sulfide more generally) at the orthopyroxene dissolution front as this front moved in the direction of fluid flow, leaving

<sup>\*</sup>Initial AIO<sub>1.5</sub> concentration defined by  $K_{An}$ .

<sup>†</sup>Values for  $K_{\text{Mg-chmt}}$  change to smaller values when chromite is >25 mode %.

behind anorthosite largely stripped of its mafic components. The result is that an increasingly chromite-rich seam develops as it collects all the Cr liberated during the formation of the replacement anorthosite. Although the model results here are developed only for thin, centimeter-scale vertical chromitite seams, there is not a practical reason why the model could not be upscaled to explain thicker and layer-parallel anorthosite-chromitite associations. In this regard, chromitites can be an excellent marker for the degree of mass loss that can occur during the solidification of the crystal pile in large layered intrusions.

Many have considered that the modest size and compositional differences between the anorthosite and norite assemblages would require the influx of magmas with different crystallization behavior (e.g. Latypov et al., 2017, 2018). However, it is suggested here that there are metasomatic processes that can occur within thick, cooling crystal mush systems and give rise to the observed features without calling upon injections of boutique magma compositions. The model presented here is broadly similar to the model proposed by Nikolaev et al. (2020) involving a silicate liquid as the metasomatic agent rather than a fluid. However, they required an anorthosite ± chromite assemblage to have been present prior to reaction, presumably crystallized from a magma. In the model proposed here, the anorthosites themselves are a replacement feature along with the chromite, both formed by the loss of pyroxene to a reactive fluid saturated in plagioclase only. The model here does have similarities to those of O'Driscoll et al. (2009) and Mathez & Kinzler (2017), but their models also envision a silicate liquid driving the metasomatism. The model for anorthosite formation presented here does have a number of similarities to the fluiddriven replacement model recently presented by Maier

Finally, ultramafic–mafic layered intrusions represent a *terra incognita* in regard to what is known about fluid composition at high temperatures and upper crustal pressures. Mineral solubility experiments are needed at the temperature–pressure conditions appropriate to the crystallization of these intrusions.

## **ACKNOWLEDGEMENTS**

This paper was markedly improved by the perceptive comments of B. O'Driscoll, E. Mathez, M Zientek, G. Costin, and an anonymous reviewer. Their time and effort are very much appreciated.

# **FUNDING**

This work was supported by a Duke University Undergraduate Research Grant (to J.S.M.) and National Science Foundation (EAR 441218 to A.E.B.).

#### **SUPPLEMENTARY DATA**

Supplementary data for this paper are available at *Journal of Petrology* online.

#### **DATA AVAILABILITY**

The data underlying this article are available in the article and in its online supplementary material.

#### REFERENCES

- Adams, J. B. (1968). Differential solution of plagioclase in supercritical water. *American Mineralogist* **53**, 1603–1613.
- Anderson, G. M. & Burnham, C. W. (1967). Reaction of quartz and corundum with aqueous chloride and hydroxide solutions at high temperatures and pressures. *American Journal* of Science 265, 12–27.
- Anderson, G. M. & Burnham, C. W. (1983). Feldspar solubility and the transport of aluminum under metamorphic conditions. American Journal of Science 283-A, 283–297.
- Antignano, A. & Manning, C. E. (2008). Rutile solubility in H2O, H2O–SiO2, and H2O–NaAlSi3O8 fluids at 0·7–2·0 GPa and 700–1000°C: implications for mobility of nominally insoluble elements. *Chemical Geology* **255**, 283–293.
- Baker, S. R. & Boudreau, A. E. (2019). The influence of the thick banded series anorthosites on the crystallization of the surrounding rock of the Stillwater Complex. *Contributions to Mineralogy and Petrology* 174, 99.
- Bastin, G. F., Dijkstra, J. M. & Heijliger, H. J. M. (1996). PROZA96: an improved matrix correction program for electron probe microanalysis based on a double Gaussian  $\varphi(\rho z)$  approach. *X-Ray Spectrometry* **27**, 3–10.
- Boudreau, A. E. (1999a). Fluid fluxing of cumulates: The J-M Reef and associated rocks of the Stillwater Complex, Montana. *Journal of Petrology* **40**, 755–772.
- Boudreau, A. E. (1999b). PELE—A version of the MELTS software program for the PC platform. *Computers & Geosciences* **25**, 201–203.
- Boudreau, A. E. (2010). The evolution of texture and layering in layered intrusions. *International Geology Review* **53**, 330–353.
- Boudreau, A. E. (2016). The Stillwater Complex, Montana—Overview and the significance of volatiles. *Mineralogical Magazine* **80**, 585–637.
- Boudreau, A. E. & McCallum, I. S. (1989). Investigations of the Stillwater Complex: Part V. Apatite as indicators of evolving fluid composition. *Contributions to Mineralogy and Petrology* **102**, 138–153.
- Cawthorn, R. G. (2015). The Bushveld Complex, South Africa.
  In: Charlier, B., Namur O., Latypov R. & Tegner, C. (eds)
  Layered Intrusions. Berlin: Springer, pp. 517–587.
- Czamanske, G. K., Zientek, M. L. & Manning, C. E. (1991). Low-K granophyres of the Stillwater Complex, Montana. *American Mineralogist* **76**, 1646–1661.
- DePaolo, D. J. & Wasserburg, G. J. (1979). Sm–Nd age of the Stillwater Complex and the mantle evolution curve for neodymium. Geochimica et Cosmochimica Acta 43, 999–1008.
- Dick, J. M. (2019). CHNOSZ: thermodynamic calculations and diagrams for geochemistry. Frontiers in Earth Science 7, 180–118.
- Fournier, R. O. & Rowe, J. J. (1977). The solubility of amorphous silica in water at high temperatures and high pressures. *American Mineralogist* **62**, 1052–1056.

- Gale, A., Dalton, C. A., Langmuir, C., H., Su, Y. & Schilling, J.-G. (2013). The mean composition of ocean ridge basalts. Geochemistry, Geophysics, Geosystems 14, 489–518.
- Hanley, J. J., Mungall, J. E., Pettke, T., Spooner, E. T. C. & Bray, C. J. (2008). Fluid and halide melt inclusions of magmatic origin in the Ultramafic and Lower Banded series, Stillwater Complex, Montana, USA. *Journal of Petrology* 49, 1133–1160.
- Helz, R. T. (1995). The Stillwater Complex, Montana: a subvolcanic magma chamber. American Mineralogist 80, 1343–1346.
- Hess, H. H. (1960). Stillwater Igneous Complex. In: *Montana—a Quantitative Mineralogical Study. Geological Society of America, Memoirs* **80**. 230 pages.
- Huang, J., Hao, J., Huang, F. & Sverjensky, D. A. (2019). Mobility of chromium in high temperature crustal and upper mantle fluids. Geochemical Perspectives Letters 12, 1–6
- Irvine, T. N. (1965). Chromian spinel as a petrogenetic indicator: Part 1. *Canadian Journal of Earth Sciences* **2**, 648–667.
- Irvine, T. N. (1967). Chromian spinel as a petrogenetic indicator: Part 2. Petrologic applications. *Canadian Journal of Earth Sciences* **4**, 71–103.
- Johnson, J. W., Oelkers, E. H. & Helgeson, H. C. (1992). SUPCRT92: a software package for calculating the standard molal thermodynamic properties of minerals, gases, aqueous species, and reactions from 1 to 5000 bar and 0 to 1000°C. Computers & Geosciences 18, 899–947.
- Jones, W. R., Peoples, J. W. & Howland, A. L. (1960). Igneous and tectonic structures of the Stillwater Complex Montana. US Geological Survey Bulletin 1071-H, 281–340.
- Kaufmann, F. E., O'Driscoll, B. & Hecht, L. (2020). Lateral variations in the Unit 7–8 boundary zone of the Rum Eastern Layered Intrusion, NW Scotland: implications for the origin and timing of Cr-spinel seam formation. *Contributions to Mineralogy and Petrology* 175, 90.
- Klemme, S., O'Neill, H. St C., Schnelle, W. & Gmelin, E. (2000). The heat capacity of MgCr<sub>2</sub>O<sub>4</sub>, FeCr<sub>2</sub>O<sub>4</sub>, and Cr<sub>2</sub>O<sub>3</sub> at low temperatures and derived thermodynamic properties. *American Mineralogist* **85**, 1686–1693.
- Labotka, T. C. & Kath, R. L. (2001). Petrogenesis of the contact-metamorphic rocks beneath the Stillwater Complex Montana. Geological Society of America Bulletin 113, 1312–1323.
- Lamy-Chappuis, B., Heinrich, C. A., Driesner, T. & Weis, P. (2020). Mechanisms and patterns of magmatic fluid transport in cooling hydrous intrusions. *Earth and Planetary Science Letters* 535, 116111.https://doi.org/10.1016/j.epsl. 2020.116111
- Latypov, R., Chistyakova, S. & Mukherjee, R. (2017). A novel hypothesis for origin of massive chromitites in the Bushveld Igneous Complex. *Journal of Petrology* 58, 1899–1940.
- Latypov, R., Costin, G., Chistyakova, S., Hunt, E. J., Mukherjee, R. & Naldrett, T. (2018). Platinum-bearing chromite layers are caused by pressure reduction during magma ascent. *Nature Communications* 9, 462.
- Maier, W. D., Barnes, S.-J., Muir, D., Savard, D., Lahaye, Y. & Smith, W. D. (2021). Formation of Bushveld anorthosite by reactive porous flow. *Contributions to Mineralogy and Petrology* 176, 10.1007/s00410-020-01760-7.
- Manning, C. E. (1994). The solubility of quartz in  $H_2O$  in the lower crust and upper mantle. *Geochimica et Cosmochimica Acta* **58**, 4831–4839.
- Mathez, E. & Kinzler, R. (2017). Metasomatic chromitite seams in the Bushveld and Rum Layered Intrusions. *Elements* 13, 397–402.

- Mathez, E. A. & Webster, J. D. (2005). Partitioning behavior of chlorine and fluorine in the system apatite–silicate melt–fluid. *Geochimica et Cosmochimica Acta* **69**, 1275–1286.
- McBirney, A. R. & Sonnenthal, E. L. (1990). Metasomatic replacement in the Skaergaard Intrusion, East Greenland: Preliminary observations. *Chemical Geology* **88**, 245–260.
- McCallum, I. S. (1996). The Stillwater Complex. In: Cawthorn, R.G. (ed.) *Layered Intrusions, Developments in Petrology 15*. Amsterdam: Elsevier, pp. 441–483.
- McCallum, I. S., Raedeke, L. D. & Mathez, E. A. (1980). Investigations of the Stillwater Complex; Part I. Stratigraphy and structure of the Banded zone. *American Journal of Science* 280-A, 59–87.
- McCallum, I. S., Thurber, M. W., O'Brien, H. E. & Nelson, B. K. (1999). Lead isotopes in sulfides from the Stillwater Complex, Montana: evidence for subsolidus remobilization. *Contributions to Mineralogy and Petrology* **137**, 206–219.
- Meurer, W. P., Klaber, S. A. & Boudreau, A. E. (1997). Discordant bodies from Olivine-Bearing zones III and IV of the Stillwater complex, Montana—Evidence for post-cumulus fluid migration in layered intrusions. *Contributions to Mineralogy and Petrology* **130**, 81–92.
- Newton, R. C. & Manning, C. E. (2000). Quartz solubility in H2O–NaCl and H2O–CO2 solutions at deep crust–upper mantle pressures and temperatures: 2–15 kbar and 500–900°C. Geochimica et Cosmochimica Acta 64, 2993–3005.
- Newton, R. C. & Manning, C. E. (2016). Evidence for SiO<sub>2</sub>–NaCl complexing in H<sub>2</sub>O–NaCl solutions at high pressure and temperature. *Geofluids* **16**, 342–348.
- Nikolaev, G. S., Ariskin, A. A. & Barmina, G. S. (2020). SPINMELT-2.0: Simulation of spinel-melt equilibrium in basaltic systems under pressures up to 15 kbar: Ill. The effects of major components in the melt on the chrome-spinel stability and a possible solution of the problem of origin of chromitites. *Geochemistry International* 58, 1–10
- Novgorodov, P. G. (1975). Quartz solubility in the H2O–CO2 mixture at 700°C and 3 and 5 kbar pressures. *Geokhimiya* **10**, 1484–1489.
- Novgorodov, P. G. (1977). On the solubility of quartz in H2O + CO2 and H2O + NaCl at 700°C and 1.5 kbar pressure. Geochemistry International 14, 191–193.
- O'Driscoll, B., Donaldson, C. H., Daly, J. S. & Emeleus, C. H. (2009). The roles of melt infiltration and cumulate assimilation in the formation of anorthosite and a Cr-spinel seam in the Rum Eastern Layered Intrusion, NW Scotland. *Lithos* 111, 6–20.
- O'Driscoll, B., Emeleus, C. H., Donaldson, C. H. & Daly, J. S. (2010). Cr-spinel seam petrogenesis in the Rum Layered Suite, NW Scotland: cumulate assimilation and *in situ* crystallization in a deforming crystal mush. *Journal of Petrology* **51**, 1171–1201.
- Orville, P. M. (1972). Plagioclase cation exchange equilibria with aqueous chloride solution: results at 700°C and 2000 bars in the presence of quartz. *American Journal of Science* **272**, 234–272.
- Parmigiani, A., Huber, C., Bachmann, O. & Chopard, B. (2011). Pore-scale mass and reactant transport in multiphase porous media flows. *Journal of Fluid Mechanics* **686**, 40–70.
- R Core Team (2019). R: A Language and Environment for Statistical Computing. R Foundation for Statistical Computing, Vienna.
- Raedeke, L. D. & McCallum, I. S. (1984). Investigations in the Stillwater Complex—Part II. Petrology and petrogenesis of the Ultramafic series. *Journal of Petrology* 25, 395–420.

- Ridolfi, F., Zanetti, A., Renzulli, A., Perugini, D., Holtz, F. & Oberti, R. (2018). AMFORM, a new mass-based model for the calculation of the unit formula of amphiboles from electron microprobe analyses. *American Mineralogist* 103, 1112–1125.
- Schiffries, C. M. (1982). The petrogenesis of a platiniferous dunite pipe in the Bushveld Complex: infiltration metasomatism by a chloride solution. *Economic Geology* 77, 1439–1145.
- Scoon, R. N. & Costin, G. (2018). Chemistry, morphology and origin of magmatic-reaction chromite stringers associated with anorthosite in the Upper Critical Zone at Winnaarshoek, Eastern Limb of the Bushveld Complex. *Journal of Petrology* 59, 1551–1578.
- Shmulovich, K. I., Graham, C. M. & Yardley, B. W. D. (2006a). Quartz, albite and diopside solubilities in  $H_2O \pm NaCl$  and  $H_2O \pm CO_2$  fluids at  $0.5 \pm 0.9$  GPa. Contributions to Mineralogy and Petrology **141**, 95–108.
- Shmulovich, K. I., Yardley, B. W. D. & Graham, C. M. (2006b). The solubility of quartz in crustal fluids: experiments and general equations for salt solutions and H2O–CO2 mixtures at 400–800°C and 0.1–0.9 GPa. *Geofluids* 6, 154–167.
- Sonnenthal, E. L. (1992). Geochemistry of dendritic anorthosites and associated pegmatites in the Skaergaard Intrusion, East Greenland: evidence for metasomatism by a chlorine-rich fluid. *Journal of Volcanology and Geothermal Research* 52, 209–230.
- Spandler, C., Mavrogenes, J. & Arculus, R. (2005). Origin of chromitites in layered intrusions: Evidence from chromite-hosted melt inclusions from the Stillwater Complex. *Geology* 33, 893–896.
- Todd, S. G., Keith, D. W., Le Roy, L. W., Schissel, D. J., Mann, E. L. & Irvine, T. N. (1982). The J-M platinum-palladium reef of

- the Stillwater Complex, Montana: I. Stratigraphy and petrology. *Economic Geology* **77**, 1454–1480.
- Veksler, I. V. & Hou, T. (2020). Experimental study on the effects of H<sub>2</sub>O upon crystallization in the Lower and Critical Zones of the Bushveld Complex with an emphasis on chromitite formation. *Contributions to Mineralogy and Petrology* **175**, 85, https://doi.org/10.1007/s00410-020-01733-w
- Volfinger, M., Robert, J.-L., Vielzeuf, D. & Neiva, A. M. R. (1985). Structural control of the chlorine content of OH-bearing silicates (micas and amphiboles). Geochimica et Cosmochimica Acta 49, 37–48.
- Walther, J. V. & Orville, P. M. (1983). The extraction–quench technique for determination of the thermodynamic properties of solute complexes: application to quartz solubility in fluid mixtures. *American Mineralogist* **68**, 731–741.
- Watenphul, A., Schmidt, C. & Jahn, S. (2014). Cr(III) solubility in aqueous fluids at high pressures and temperatures. *Geochimica et Cosmochimica Acta* 126, 212–227.
- Waters, C. & Boudreau, A. E. (1996). A re-evaluation of crystal size distribution in chromite cumulates. *American Mineralogist* **81**, 1452–1459.
- Weill, D. F. & Fyfe, W. S. (1964). The Solubility of Quartz in  $H_2O$  in the range 1000–4000 bars and 400–550 °C. *Geochimica et Cosmochimica Acta* **28**, 1243–1255.
- Yardley, B. W. D. (2005). Metal concentrations in crustal fluids and their relationship to ore formation. *Economic Geology* **100**, 613–632.
- Yoder, H. S. & Tilley, C. E. (1962). Origin of basalt magmas: an experimental study of natural and synthetic rock systems. *Journal of Petrology* **3**, 342–532.